Review article

Cristina I. Øie[a], Viola Mönkemöller[a], Wolfgang Hübner, Mark Schüttpelz, Hong Mao, Balpreet S. Ahluwalia, Thomas R. Huser and Peter McCourt*

New ways of looking at very small holes – using optical nanoscopy to visualize liver sinusoidal endothelial cell fenestrations

https://doi.org/10.1515/nanoph-2017-0055
Received May 16, 2017; revised September 27, 2017; accepted October 30, 2017

Abstract: Super-resolution fluorescence microscopy, also known as nanoscopy, has provided us with a glimpse of future impacts on cell biology. Far-field optical nanoscopy allows, for the first time, the study of sub-cellular nanoscale biological structures in living cells, which in the past was limited to electron microscopy (EM) (in fixed/dehydrated) cells or tissues. Nanoscopy has particular utility in the study of "fenestrations" – phospholipid transmembrane nanopores of 50–150 nm in diameter through liver sinusoidal endothelial cells (LSECs) that facilitate the passage of plasma, but (usually) not blood cells, to and from the surrounding hepatocytes. Previously, these fenestrations were only discernible with EM, but now they can be visualized in fixed and living cells using structured illumination microscopy (SIM) and in fixed cells using single molecule localization microscopy (SMLM) techniques such as *direct* stochastic optical reconstruction microscopy. Importantly, both methods use wet samples, avoiding dehydration artifacts. The use of nanoscopy can be extended to the *in vitro* study of fenestration dynamics, to address questions such as the following: are they actually dynamic structures, and how do they respond to endogenous and exogenous agents? A logical further extension of these methodologies to liver research (including the liver endothelium) will be their application to liver tissue sections from animal models with different pathological manifestations and ultimately to patient biopsies. This review will cover the current state of the art of the use of nanoscopy in the study of liver endothelium and the liver in general. Potential future applications in cell biology and the clinical implications will be discussed.

Keywords: liver; endothelium; optical nanoscopy; fenestration.

1 Why we need optical super-resolution for liver research

The "tyranny of distance" was once used to describe the difficulties associated with geographical distances between continents prior to the incredible developments in transportation and electronic communications. The science of optics has a similar "tyranny of distance", namely, the approximately 200 nm optical diffraction limit of visible light. This limit prevents our use of conventional light microscopy to study a number of highly relevant biological structures, such as cellular fenestrations (cellular pores ≤150 nm diameter that allow free passage of molecules through cells), viruses (usually ≤100 nm), and nanoparticles. All of these structures are especially relevant to our livers – in particular for a fenestrated liver cell with a voracious appetite for waste molecules, viruses, and nanoparticles, namely, the liver sinusoidal endothelial cell (LSEC). Every day LSECs remove huge amounts of waste, nanoparticles, and viruses from the blood. Blood-borne fats or lipids pass through LSEC fenestrations to be removed and processed by underlying hepatocytes. Pharmaceuticals also

[a]**Cristina I. Øie and Viola Mönkemöller:** These authors contributed equally to this work.
***Corresponding author: Peter McCourt,** University of Tromsø – The Arctic University of Norway, Department of Medical Biology, MH Building, 9037 Tromsø, Norway, e-mail: peter.mccourt@uit.no; peter.mccourt@sydney.edu.au. http://orcid.org/0000-0001-5072-4590
Cristina I. Øie and Balpreet S. Ahluwalia: University of Tromsø – The Arctic University of Norway, Department of Physics and Technology, Technology Building, 9037 Tromsø, Norway
Viola Mönkemöller, Wolfgang Hübner, Mark Schüttpelz and Thomas R. Huser: Bielefeld University, Department of Physics, Universitätsstr. 25, 33615 Bielefeld, Germany. https://orcid.org/0000-0001-5338-1706 (M. Schüttpelz)
Hong Mao: University of Tromsø – The Arctic University of Norway, Department of Medical Biology, MH Building, 9037 Tromsø, Norway

need to pass through these fenestrations to be activated (e.g. cholesterol-reducing statins) or detoxified by hepatocytes. And, when we age, our LSEC fenestrations become smaller and fewer, as they also do in various liver disease states [1]. Today, we study these cells and structures using either conventional diffraction limited light microscopy on living cells or high-resolution (but static) methods such as transmission and scanning electron microscopy (EM) on fixed (i.e. dead) tissue. Such methods, while very powerful, yield no real-time information about the uptake mechanisms nor any information about fenestration dynamics (i.e. are they static, or do they open and close?). Therefore, to study LSECs, we are now able to use novel super-resolution optical methods and to also develop our own tools, to map their functions in four dimensions.

This review will describe the challenges of studying LSECs by light microscopy, as well as current and potential future solutions to this challenge. We will summarize the diffraction-unlimited super-resolution light microscopy techniques, now termed "optical nanoscopy", and their application particularly in the study of the liver and its fenestrated endothelium and discuss the opportunities for and challenges associated with each technique.

2 Liver morphology and functions

The liver is the largest internal organ of the body representing approximately 2–5% of the total body weight. Macroscopically, the organ consists of two main lobes, each divided into eight segments with independent vascular and duct supply. About 25% of the liver's blood supply comes from the hepatic artery, with the remainder coming via the portal vein, which comprises nutrient-rich blood

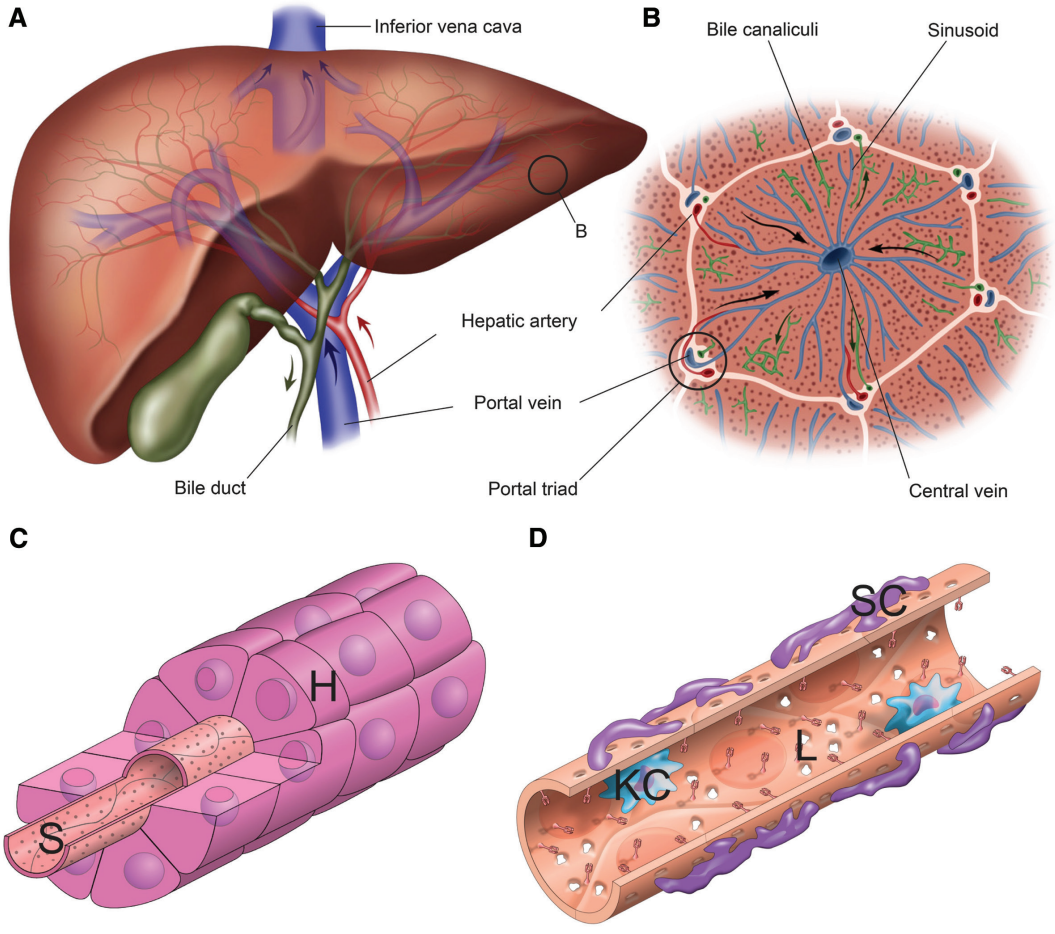

Figure 1: Liver anatomy.
(A) Entire organ and blood supply. Blue indicates venous blood, red indicates arterial blood, green indicates bile. (B) Liver lobule showing rows of hepatocytes radiating out from the central vein towards the portal triad. (C) Hepatocytes (H) in close contact with the sinusoid (S). (D) Arrangements of the sinusoidal cells in the sinusoid: L, LSEC; SC, stellate cell; KC, Kupffer cell. Figures 1A and B are adapted and used with permission from Illustrated Verdict (illustratedverdict.com). Figures 1C and D are courtesy of D'Liver (dliver.com) and used with permission.

from the gastrointestinal tract, pancreas, and spleen [2] (Figure 1A). The organ is essential for maintaining homeostasis and metabolic integrity in the body; harboring important functions associated with regulation of carbohydrate, lipid, amino acid, and hormone metabolism; synthesis and degradation of plasma proteins; glycogen synthesis; storage of vitamins and metals; secretion of bile; and xenobiotic metabolism among others [3, 4]. Hepatic lobes are divided into thousands of microscopic units called lobules which are roughly hexagonal in shape, consisting of rows of hepatocytes radiating out from a central vein (Figure 1B). The apical domain of hepatocytes is adjacent to canaliculi into which bile is secreted, while their basal domain is in near contact with the liver sinusoids (Figure 1C), which are capillaries through which blood from the hepatic portal vein and hepatic artery enters via the portal triads, then drains into the central vein and is transported out of the liver [5]. The sinusoids have a diameter of approximately 5–10 μm [6, 7], and their walls consist of a single layer of LSECs, a specialized type of endothelium that differs both structurally and functionally from other endothelia [8, 9]. Hepatic stellate cells (SCs), the vitamin A storing units, are located in the perisinusoidal space (the space of Disse), between the sinusoid and the hepatocytes [4], whereas Kupffer cells (resident macrophages) and resident lymphocytes are located on the luminal side of the sinusoidal lining [10, 11] (Figure 1D).

LSECs are characterized by unique morphological and functional features. In general, the sinusoidal endothelium of the normal liver is very thin, ranging between 150 and 170 nm in young individuals [12], and their extended cytoplasm contains numerous transmembrane pores, called fenestrae, with diameters ranging from 50 to 150 nm [9, 13]. The fenestrae lack a diaphragm and are usually clustered together in groups, called "sieve plates" [9, 14] (Figure 2). Individual fenestrations can also be seen scattered across the endothelial surface or in labyrinth-like structures [16, 17]. LSECs lack a basal lamina; thus, the circulating plasma macromolecules have direct access to the subendothelial hepatocytes via the space of Disse. In addition to their filtration function, another functional characteristic of LSECs is their superefficient endocytic capacity and lysosomal degradation, making them among the most effective scavengers of blood-borne waste macromolecules in the body [1]. Sinusoidal endothelial function is affected in various pathological conditions when LSECs undergo morphological and functional transformations. One of the most remarkable phenotypic changes is the loss of fenestrations along with the formation of a basement membrane [18]. In fact, LSEC defenestration, often accompanied with basement membrane synthesis and altered surface marker expression resulting in "capillarization" of the sinusoids, is a ubiquitous clinical manifestation observed in various liver diseases such as fatty liver [19], cirrhosis [20], primary biliary cirrhosis [21], hepatitis [22], specific viral infection of LSECs [23], and with the venous administration of endotoxin [24]. A form of capillarization (fenestration loss, basement membrane deposition) of the liver sinusoids also occurs during aging, termed "pseudocapillarization" [12, 25–32]. These age-related morphological changes are accompanied by altered expression of many vascular proteins including von Willebrand's factor, ICAM-1, laminin, caveolin-1, and various collagens [33]. However, these changes occur without age-related pathology of hepatocytes or activation of SCs [34] typically seen in diseased livers.

To study fenestrations and (pseudo-)capillarization phenomena, microscopy techniques below the optical resolution limit need to be utilized. Until recently, visualization of fenestrations has been limited to EM (Figure 2A and B), with Eddie Wisse being the pioneer in the field, who described in detail the ultrastructure of the LSEC in 1970 [14]. EM, which uses electrons instead of photons, is able to achieve up to 100× greater resolving power than conventional light microscopy. However, transmission and scanning EM techniques are technically demanding, relatively costly, time-consuming, and incompatible with studying living cells or tissues. The samples must undergo a series of fixation and dehydration steps that generate artifacts, such as shrinkage of the specimen and alteration of tissue structure [35]. This may explain why the average diameter of the fenestrations, measured to be 150–175 nm by transmission electron microscopy (TEM), was found to be 105–110 nm by scanning electron microscopy (SEM) in the same study [36]. Atomic force microscopy (AFM) is another technique widely used to study the membrane topology of various fixed cells [37]. Membrane probing of living cells using AFM has proven to be more challenging due to the limitations in temporal resolution (i.e. AFM acquisition speed) and the high local pressure exerted by the tip. So far, time-lapse studies of LSEC fenestrae by AFM have been very limited [38, 39], with one very recent study showing detailed fenestration morphology [40]. Over the last decade, several super-resolution optical microscopy methodologies have been developed that allow optical resolution beyond the diffraction limit [41–45]. They can be classified into three broad classes: those based upon structured illumination microscopy (SIM) (Figure 2C and D), those based upon point spread function (PSF) engineering, and those based upon localization of individual fluorophores, commonly referred to as single molecule localization microscopy (SMLM) (Figure 2E and F).

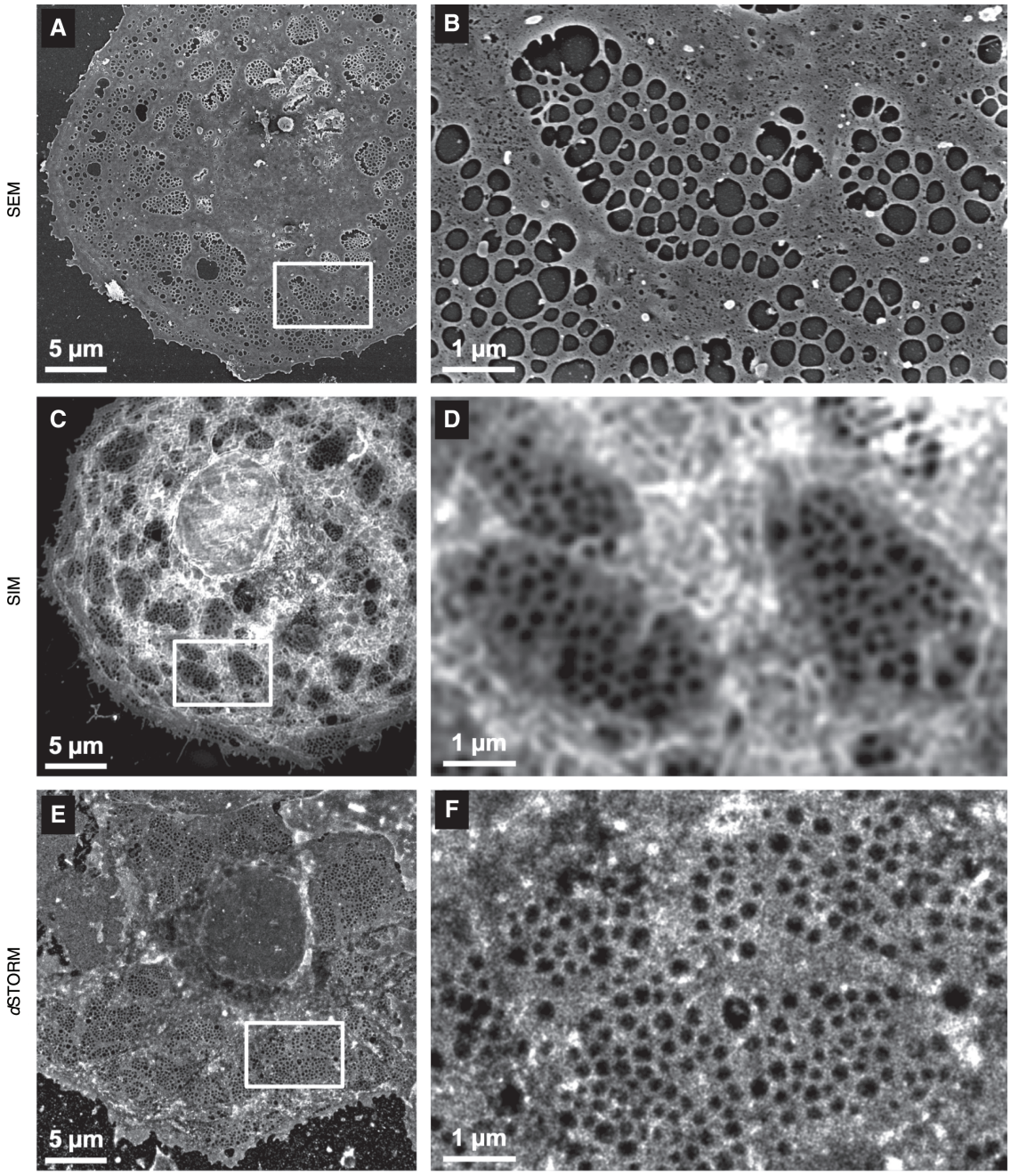

Figure 2: Liver sinusoidal endothelial cell (LSEC) at high resolution.
(A) Scanning electron microscopy (SEM) of a representative LSEC, (C) structured illumination microscopy (SIM) and (E) direct stochastic optical reconstruction microscopy (*d*STORM) of similar cells. (B), (D), and (F) are magnifications of the regions highlighted in (A), (C) and (E), respectively, showing several sieve plates containing numerous fenestrations. (C)–(F) are adapted from [15].

3 Optical super-resolution imaging methods

The resolution of an optical microscope is fundamentally limited by diffraction. Ernst Abbe originally described this diffraction limit of optical resolution in 1873 [46]. The resolution is proportional to the wavelength (λ) of the light used for imaging an object and inversely proportional to the maximum acceptance angle at which an objective lens can collect light. This angle is defined by the numerical aperture ($\mathrm{NA} = n \cdot \sin(\alpha)$, where n is the refractive index of the immersion medium and α the half collection angle) of the objective lens:

$$d = \frac{\lambda}{2n\sin\alpha} = \frac{\lambda}{2\mathrm{NA}}$$

Equation 1: The Abbe equation. Laser scanning confocal microscopes can improve the spatial resolution up to a factor of √2 by using the same excitation and detection optics, including a pinhole in the detection path [47]. Optical super-resolution techniques, however, circumvent the Abbe limit to produce images with a spatial resolution beyond the diffraction limit.

3.1 Super-resolution structured illumination microscopy

Super-resolution structured illumination microscopy (SR-SIM) (reviewed in [48]) is a wide-field microscopy approach employing coherent spatial modulation of the excitation light to provide a two-fold resolution improvement. In contrast to other super-resolution methods, it does not rely on special properties of the fluorophores as it only requires a linear, incoherent response to the excitation light intensity. Two-dimensional (2D) SR-SIM was first demonstrated by Heintzmann and Cremer [49] and Gustafsson [45]. In 2008, Gustafsson et al. [50] then expanded the technique to three dimensions (3D).

The SR-SIM process relies on mixing of the structured illumination pattern with a known frequency and the structure of the sample with unknown frequency, resulting in a pattern comparable to Moiré fringes. Higher frequency components become detectable as the difference-frequency mixing with the illumination pattern shifts them into the resolvable frequency band. Reconstruction algorithms retrieve this super-resolved information and compute an image with doubled spatial resolution.

To recover the original sample frequencies, the stripes of the illumination pattern have to be moved across the sample in evenly spaced phase steps for a given angle. An image is then taken at each phase position. That way, higher resolution information is collected in the direction of the phase translation. The acquisition of phase shifts is repeated for different evenly spaced angles by rotating the interference pattern to gain an isotropic resolution enhancement.

The SIM reconstruction process is best understood by studying images in Fourier (frequency) space. A 2D Fourier representation (power spectrum) of a real space image shows spatial frequencies within a circular pattern (Figure 3, wide-field image and corresponding Fourier transform). Fine details of the image will appear as high frequencies near the border of this circle, while coarse details result in lower frequencies close to the center. The maximum radius of the circular pattern (shown in yellow) is defined by the resolution limit [Eq. (1)], i.e. higher resolution leads to a larger circle and thus higher resolved frequencies.

In SR-SIM raw images, higher frequency information is down-modulated to lower frequencies. As seen in Figure 3 (SIM raw data and Fourier space angles 1–3), this super-resolved information is entangled within the resolvable frequencies. Reconstruction algorithms extract these data and shift it back to their correct position in frequency space. The final image is then obtained after combining the information for each angle (Figure 3, Fourier space of SR-SIM reconstruction) and subsequent reverse transform from Fourier space to real space (Figure 3, SR-SIM reconstruction).

Linear SR-SIM can be utilized in 2D as well as in 3D. For 3D imaging, a structured illumination pattern is generated axially by three-beam interference [50]. This results in 2 times improved optical sectioning. To reconstruct 3D data sets, a total of 15 images per focal plane are needed. The quality of the final super-resolution image relies on the quality of the software implementation of the SR-SIM reconstruction algorithm. Reconstruction artifacts can be mitigated by careful instrument calibration and sample preparation. Recent open-source software tools permit additional quality assessment of the recorded raw data and possible different reconstruction parameter options [52, 53].

3.2 Single molecule localization microscopy

In 2006, three research groups independently developed similar optical super-resolution methods with a lateral sub-diffraction resolution of around 20 nm. While Betzig and collaborators [43] termed their method “photoactivated localization microscopy” (PALM), Hess and colleagues from the University of Maine called it “fluorescence photoactivation localization microscopy” (fPALM) [54]. Zhuang and collaborators [55] from Harvard University developed STORM: “stochastic optical reconstruction microscopy”. In 2014, the Nobel Prize in Chemistry was jointly awarded to Eric Betzig, Stefan Hell, and W.E. Moerner “for the development of super-resolved fluorescence microscopy”. As early as 1995, Betzig [56] proposed the general principle of isolating and localizing single fluorescent molecules in a crowded environment, one of the foundations of far-field optical super-resolution microscopy. All other methods of localization microscopy are therefore considered specific embodiments. These

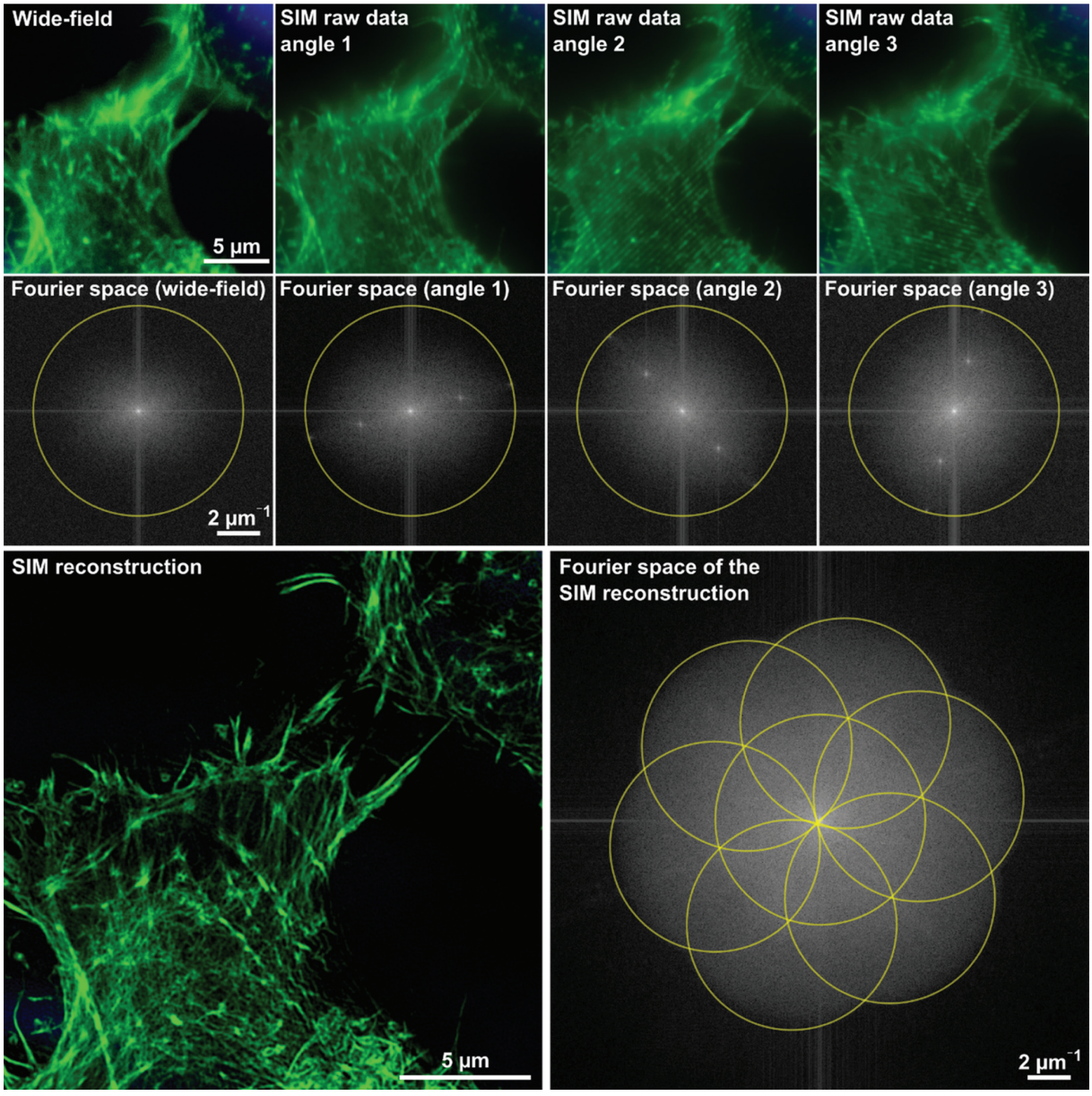

Figure 3: The principle of SIM.
Top row: micrograph images of U2OS cells stained for actin filaments (Phalloidin-ATTO488) acquired with a 3D-SIM in wide-field mode and SIM raw images at different angle orientation of the illumination pattern (1–3). Second row: Corresponding graphic representations of the Fourier transforms that show the frequency information. Bottom row: 3D-SIM reconstruction and the corresponding frequency space representation. In this visualization, low frequency components are centered, high frequency extends to the sides of the image. The strength and the cut-off of these frequency components indicate the increased resolution achieved by SIM compared to wide-field. Adapted from [51].

techniques have in common that they use effective means (temporal fluctuations, spectral distinctiveness, and photoswitching) to determine if indeed a single molecule is being probed. The position of the molecule can then be estimated very precisely through the carefully characterized PSF of the optical microscope. Multiple localizations of single molecules obtained in a series of images, usually hundreds to thousands, are then used to form a super-resolved image.

The efficacy of this method can be further improved by the use of photoactivatable or photoswitchable fluorescent proteins or fluorophores. Here, the molecules are switched between a fluorescent bright ("on") and a non-fluorescent dark ("off") state either upon illumination with light of different wavelengths (PALM/STORM) or photoactivation and photobleaching (fPALM). fPALM uses fluorescent proteins such as the photoactivatable green fluorescent protein (PA-GFP), while PALM additionally

makes use of photoswitchable proteins, e.g. the green fluorescent protein Dronpa [57]. In turn, the first fluorophores that were used for STORM were coupled carbocyanine fluorophores [55], which exhibit photoswitching properties in the presence [58] or absence of a so-called "activator molecule" [59]. The need for coupling these organic fluorophores was soon thereafter removed by the introduction of special buffer systems that serve a similar purpose. The latter method is therefore called *direct*-STORM (*d*STORM).

3.2.1 *direct* Stochastic optical reconstruction microscopy

*d*STORM utilizes the photoswitching properties of commercially available fluorophores, which can be achieved by irradiating the sample with either one [60] or two [61] wavelengths of light and an appropriate buffer condition [62]. The switching to the non-fluorescent ("off") state is triggered by the same wavelength that also excites the molecule's fluorescence for localization. The fluorescent ("on") state can be reversibly recovered by the use of laser light at lower wavelength regions, such as 405 nm or 488 nm. For efficient photoswitching of fluorophores specifically engineered for single molecule detection (i.e. fluorophores exhibiting high fluorescence quantum yield, high photostability, and minimal intrinsic "blinking"), controlling the oxygen content in the buffer medium with an enzymatic oxygen scavenging system (OSS) as well as adding thiolated small molecules to the buffer medium permits almost seamless adjustment of the rates at which photoswitching occurs [63]. This leads to a dramatically improved reversibility of the photoswitching process that is required for significant high localization statistics.

In SMLM a small subset of all fluorophores attached to the structure of interest is activated at any time (Figure 4A and B), effectively confining the fluorescence emission of the activated fluorophores (Figure 4C). A fast and low-noise camera capable of exposure times in the millisecond range is used for image acquisition. High-precision localization with nanometer accuracy is then performed for each fluorescent spot detected in each individual image (Figure 4D) [64]. A sequence of several hundreds to thousands of fluorescence images ("image stack") is recorded using illumination of an entire field of view (f-o-v). The specific illumination mode, [e.g. wide-field or total internal reflection fluorescence (TIRF) illumination, or the use of light sheets, to name just a few examples] is typically adapted to the specific experimental requirements [65]. All localized fluorophores are subsequently combined to form one super-resolved image that is able to resolve structures down to 20 nm (Figure 4E).

3.2.2 Localization of single fluorophores

The resolution of a super-resolved image is (among others) given by the localization precision of a single molecule. The localization precision is dominated by photon statistics, i.e. the Poisson distribution of emitted photons [64], and it depends on the number of photons emitted by a fluorophore if background noise is negligible. The standard error in the fitted fluorophore position, i.e. the localization precision, can then be written as $\sigma/\sqrt{N}$, where σ is the standard deviation of the PSF of the experimental setup that is frequently approximated by a Gaussian function, and N is the number of detected photons emitted by the fluorophore. To obtain a localization precision of 10 nm using a high-NA objective lens, more than 1000 photons have to be detected from one fluorophore within a data acquisition time in the millisecond range. For a precision of only a few nanometers, approximately 10,000 photons have to be collected. Due to switching and bleaching of fluorophores, only several hundred photons effectively reach the detector such that an accuracy of around 20 nm is expected for most experiments. The use of Gaussian fitting to determine the location of a single

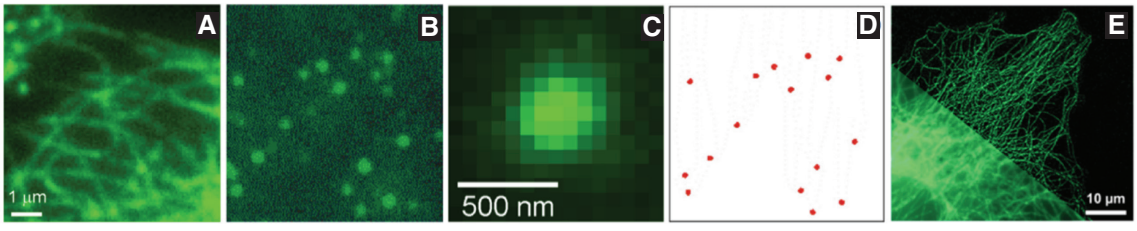

Figure 4: The principle of *d*STORM.
(A) Conventional image of the cellular microtubule network, (B) selective activation of a small subset of fluorophores attached to the sample, (C) diffraction limited image of a single molecule, (D) localization of single molecule position using 2D Gaussian function, and (E) comparison of conventional TIRF (lower left part) to *d*STORM image (FWHM 21 nm).

molecule is just one example of a large number of localization methods, such as maximum likelihood estimation of various models, etc. For a comprehensive review, see e.g. Deschout et al. [65].

Besides finding the appropriate chemical environment optimal for photoswitching depending on the fluorophore and the sample, data processing is a challenging task. The acquired image stack needs to be processed quickly and accurately. The major drawback of this method is that the computational effort of localizing the fluorophores with nanometer precision requires significant computation power. Data acquisition and processing times can, hence, limit fast and real-time applications. Fast and robust image processing algorithms for localizing fluorophores with nanometer accuracy, such as rapidSTORM [66, 67] and ThunderSTORM [68], were developed using only a few assumptions and simplifications. RapidSTORM is available as a stand-alone executable program, while ThunderSTORM comes as a plug-in for ImageJ. Additionally, many other software packages are available [69]. Code optimization and the use of computers with multicore central processing units, as well as acceleration through the use of graphics processing units, have enabled real-time data fitting [66, 67], even for more complex algorithms [70–73].

3.3 Stimulated emission depletion microscopy

Stimulated emission depletion (STED) microscopy relies on Einstein's concept of stimulated emission. The concept of using stimulated emission as a means of improving the spatial resolution of optical microscopy in the far field beyond Abbe's diffraction limit was first proposed by Hell and Wichmann in 1994 [41]. It then took almost 6 years to experimentally demonstrate that this theoretical concept does, indeed, enable one to overcome the diffraction limit, when Klar et al. [74] were able to show a narrowing of the axial resolution from approximately 600 nm to about 100 nm by generating high intensity depleting laser spots just above and below the fluorescence excitation focus of a laser scanning confocal microscope. The concept relies on the fact that a molecule in an electronic excited state has several competing pathways through which it can relax back to the electronic ground state. The most frequently observed pathway depends on the spontaneous emission of a fluorescent photon, the rate of which is primarily ruled by the excited state lifetime. In the absence of external fields, molecules can also relax through triplet states and by thermal means, albeit at much lower rates. However, as Einstein showed and as realized in the laser, the presence of a strong, resonant electromagnetic field that fulfills several important attributes (i.e. wavelength, propagation vector, polarization, etc.), can also induce the transition of a molecule from the excited state to the ground state and leads to the emission of a photon with those same attributes. This mechanism has several important properties that allow it to be exploited in STED microscopy. First, the emission is induced, i.e. instantaneous, and does not depend on the excited state lifetime. Also, rather than the broad emission spectrum obtained by spontaneous emission, STED emission is monochromatic at the same wavelength used for the induction of the process. And, most importantly, the dependence of the process on the intensity of the laser beam inducing the transition is highly nonlinear [75]. Thus, by overlapping a laser beam with a wavelength within the emission spectrum of a fluorescent molecule with a confocal laser beam that excites fluorescence, a number of molecules in the excited state can be forced back to the ground state by stimulated emission. This introduces non-linearity as the emission begins to saturate above a certain intensity of the stimulating laser beam. Blocking the wavelength at which stimulated emission occurs, e.g. by a narrow notch filter, enables one to still collect the spontaneous fluorescence signal of the molecules remaining in the excited state. By shaping the STED beam, ideally in the form of a donut, where the centroid of the donut overlaps with the centroid of the confocal excitation beam, the nonlinear dependence of STED leads to a spatial narrowing of the molecules that remain in the excited state to a region in the very center of the donut beam. This concept has several important advantages: it enables "scaling" of the spatial resolution depending on the intensity of the STED beam. This has been advantageously exploited in STED fluorescence correlation spectroscopy, which has, e.g. allowed Eggeling and coworkers to determine diffusion rates of constituents of the cellular plasma membrane across multiple length scales well below the optical diffraction limit [76]. Also, another important advantage is that STED, implemented in a laser scanning microscope, produces "instant" super-resolution, meaning that no additional image processing is needed in order to obtain a super-resolved fluorescence image. A disadvantage, however, is the fact that in order to fully suppress spontaneous emission from the excited state, rather high STED powers are required, which is often detrimental to sample health. Here, the combination with photoswitchable fluorophores, as realized in "REversible Saturable Optical Linear Fluorescence Transition" (RESOLFT, i.e. photoswitching with low power), has significantly reduced

this dependence at the expense of increased sample preparation [77].

3.4 Non-linear SR-SIM imaging

All of the applications of SR-SIM applied to LSECs, as well as the vast majority of SR-SIM applications related to a biological or biomedical research problem, utilize the linear implementation of SR-SIM. Linear SR-SIM means that the illumination pattern is purely a cosine-like interference pattern with gently rising slopes, leading to at most a doubled spatial resolution. As early as 2002, Heintzmann et al. had, however, already pointed out that SR-SIM is not conceptually or fundamentally limited to a mere doubling of its spatial resolution [78]. Gustafsson in 2005 first demonstrated nonlinear (NL-)SIM using the process of fluorescence saturation [79]. The source of fluorescence in organic fluorophores is the electronic excited state with a limited lifetime of a few nanoseconds. The excited state becomes more and more populated at high excitation intensities, because the probability for transferring an electron from the ground state to the excited state continues to rise linearly with the excitation intensity. The finite time that the electron spends in the excited state, however, prevents rapid depopulation. The fluorescence signal will therefore no longer linearly respond to the excitation power and begins to approach a maximum value. This saturation effect introduces a nonlinearity into fluorescence excitation, which could, in principle, be used for non-linear structured illumination microscopy (NL-SIM). A caveat of this mechanism is that the more time molecules spend in the excited state, the more of them will undergo irreversible photobleaching. Also, high excitation powers at visible wavelengths are typically detrimental to the health of biological samples, posing yet another limitation. While these issues are most relevant for live imaging, it should be pointed out that there is also a potential link between fluorescent staining and high excitation powers with regard to sample health as unstained samples are often more likely to survive exposure to high laser powers. This is related to the formation of free radicals by fluorescence excitation, which can often be minimized but never entirely avoided [80]. Nonetheless, by carefully controlling experimental conditions, i.e. by using a high power, Q-switched diode laser and adjusting its repetition rate to the camera exposure time, Gustafsson was able to keep these effects to a minimum, and he demonstrated the detection of 50 nm beads by NL-SIM with a resolution of 49 nm. In order to extract the additional higher order harmonics from the limited support of the optical transfer function (OTF), images at nine different phases and 12 different angles had to be collected, resulting in 108 images to be processed by the SR-SIM reconstruction algorithm. In this experiment, the same pattern was used to induce the nonlinear saturated excited state and to excite fluorescence. Other than the pulsed diode laser and requiring more and smaller phase steps and angles, no further modifications were made to the SR-SIM instrument [79]. In principle, this approach could be applied to imaging samples with more robust, non-bleaching fluorophores, such as nanodiamonds or quantum dots, but biological applications have, so far, not been demonstrated with this implementation of NL-SIM.

In the search for more biology-friendly approaches to NL-SIM, the group of Mats Gustafsson next set their eyes on other types of fluorophores that provide an intrinsic nonlinear optical response, which could be utilized at lower excitation power levels. This was demonstrated by Rego et al. in 2012, where they utilized a photoswitchable protein, combined with 2D TIRF-SIM to obtain similar spatial resolution as in the prior use of saturated fluorescence excitation [81]. Again, by carefully characterizing the photoswitchable protein Dronpa, a condition was found that allowed them to switch Dronpa between a nonfluorescent “off” state and a fluorescent “on” state between 60 and 70 times. Here, the NL-SIM image acquisition process required three consecutive exposures of the sample. First, all Dronpa molecules were switched to the “on” state by applying uniform illumination of the sample at 405 nm wavelength. Then, a sinusoidal excitation pattern was used to turn the molecules off – the duration and power of which was used to control the saturation of this process, such that only narrowly confined strips of molecules along the minima of the cosine pattern remained in the on state. Then, after shifting the phase of the excitation pattern by π, the fluorescence of the molecules remaining in the on state was collected. This process required only seven phase steps and nine different angles or 63 images in total to be collected in order to extract the information of two higher orders, resulting in the imaging of the cytoskeleton and nuclear pores in fixed cells with approximately 60 nm resolution across the entire f-o-v [81]. The authors already mention in this paper that as few as five phases and five angles, resulting in 25 images, could be used to detect these two higher orders.

More recently, Li et al. demonstrated an impressive improvement of NL-SIM by extending it to live cell applications. Several changes were made to the previous procedures: an increased NA of the objective lens readily extended the spatial resolution of TIRF-SIM to well

below 100 nm. This enabled the rapid imaging of endocytic uptake processes and cytoskeletal changes in cells with 84 nm spatial resolution for up to 100 time points (i.e. final reconstructed, super-resolved images) [82]. By utilizing the green photoswitchable fluorescent protein Skylan-NS, NL-SIM was implemented in TIRF mode. Here, a 1.57 NA TIRF lens was used rather than the 1.7 NA TIRF lens, because the index oil used as immersion fluid for the 1.7 NA objective lens was found to absorb blue light at 405 nm. The image acquisition procedure was also changed, such that fluorophores were kept in the off state. Exposure of a small part of the sample to a sinusoidal activation pattern at 405 nm was then followed by a carefully controlled excitation pattern at 488 nm. Here, the two sinusoidal standing wave patterns had to be modified such that they precisely overlapped in TIRF mode across the entire f-o-v. This overlap between the patterns increased the nonlinearity of the process, allowed for low activation and excitation intensities, and kept the number of molecules present in the excited state to a minimum, all of which prolonged the lifetime of the sample and reduced phototoxicity. With this procedure, as few as 25 images (5 phase × 5 angles), as well as the use of a high NA objective lens, were sufficient to reconstruct images of living cells approaching 60 nm spatial resolution. It should be noted, however, that utilizing this minimum number of images, as well as the low signal-to-noise ratio of this imaging procedure, results in stronger image reconstruction artifacts of the final images [83, 84]. Improvements to the image reconstruction algorithm or filters used to reconstruct NL-SIM images should, however, help reduce these effects in future implementations [85, 86]. Notably, by implementing the principles of NL-SIM to lattice light sheet microscopy, the resolution of this imaging method could also be improved in 3D, albeit not in all three directions at the same time [82]. Although the implementation of NL-SIM is more complex than standard SR-SIM, requiring the use of special, photoswitchable dyes imaged by a SIM microscope providing for precise pattern alignment, we expect this method to witness rapid growth in the near future.

4 Optical nanoscopy and liver sinusoidal endothelial cells

Until 2010, imaging of characteristic LSEC substructures (fenestrations) was possible only by TEM, SEM, and AFM with their respective downsides already mentioned above. Optical fluorescence microscopy is a more suitable method, because it enables the fast, high throughput observation of wet samples with modest preparation steps. For this purpose, however, the molecules of interest have to be specifically labeled with fluorophores.

Conventional fluorescence microscopy such as deconvolution of 3D wide-field images or confocal laser scanning microscopy (LSM) are widely used in cellular and molecular biology studies. Since LSEC fenestrations have diameters of ≤150 nm that are arranged in sieve plates with diameters of just a few microns, microscopy techniques used for the investigation of these structures must therefore be capable of resolving these tiny features of interest. The resolution of the LSM, even in combination with deconvolution, is not sufficient to resolve single fenestrations, as shown in Figure 5. The optical resolution (at a detection wavelength of 500 nm) ranges between 132 and 182 nm depending on the pinhole size.

Optical nanoscopy has up to now only been applied to distinct cultures of isolated LSECs on coverglass coated with collagen or fibronectin. Isolated LSECs are highly adherent to the substrate, and within 2 h from seeding, they appear round in shape and with a very flat and thin cytoplasm about and above the bulging nucleus.

4.1 SR-SIM applied to LSECs

Cogger et al. [87] first showed that super-resolved SIM offers the possibility to investigate LSECs. The spatial resolution of linear SR-SIM reaches about 100 nm (lateral) in the best case. Since SR-SIM utilizes standard fluorescent microscopy protocols or even non-bleaching, non-fluorescent surface-enhanced Raman scattering (SERS) particles [88], SR-SIM is ideally suited for biological systems that are difficult to use in conjunction with fluorescent proteins.

SR-SIM was used to first visualize fenestrations and their distribution in sieves plates in isolated rat LSECs. For this purpose the cell membranes were labeled with CellMask Orange after cellular fixation. This dye results in fairly uniform staining of the plasma membrane. On fixed samples, it will also incorporate into all intracellular lipid membranes.

The measured average fenestration diameter of 123 ± 24 nm was similar to the sizes and structure obtained from scanning EM studies [87]. Diameters as small as 69 nm were measured. The distribution of the fenestrations in sieve plates corresponds to the very thin cellular areas distinct from the thicker cytoplasmic volume surrounding the nucleus.

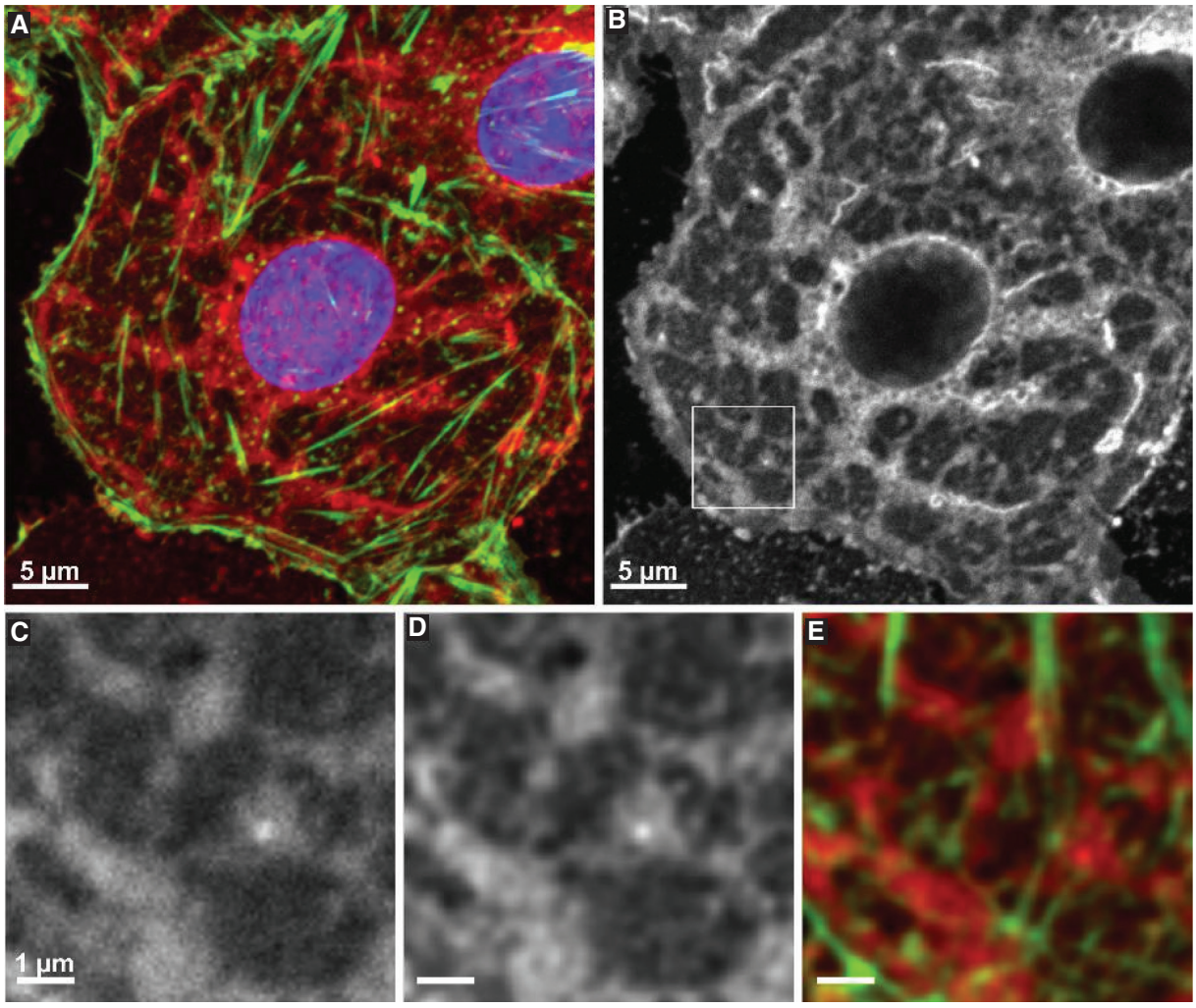

Figure 5: Confocal microscopy images of rat LSEC.
Zeiss LSM780 image of an entire isolated rat LSEC (A) with stained nucleus (blue, DAPI), actin (green, Phalloidin-ATTO488), and membrane (red, CellMask Orange; pinhole: 0.6 AU). In (B) only the membrane channel of the same image is shown. The region of interest (ROI) (dashed box) is enlarged in (C) for the membrane LSM raw data as well as in (D) for the deconvolved LSM data (E) shows an overlay of the deconvolved actin and membrane channels from that ROI area. Taken from [51].

Furthermore, the previously speculated tight interaction between the actin cytoskeleton and the fenestrations distributed into sieve plates was imaged [87, 89]. While thin actin filaments surround fenestrations, thick bundles and tubulin form rings around the sieve plates. Endothelial nitric oxide synthase, a potential key protein for the regulation of fenestrations, appeared to colocalize with the actin cytoskeleton surrounding but not within the sieve plates [87]. 3D-SIM was further used to assess the localization of lipid raft associated stain Bodipy FL C5 ganglioside GM1 in rat LSECs. Rafts appeared preferentially distributed in the perinuclear regions of LSECs while not being present in sieve plates. These SIM observations lead to the postulation that fenestrations form in non-raft regions and diminished actin filament supported regions of LSECs [90].

4.2 Direct stochastic optical reconstruction microscopy applied to LSECs

Recently, Mönkemöller et al. [15] applied *d*STORM to LSECs to gain deeper insight into the structural details of fenestrations in LSECs in an aqueous environment. *d*STORM enables 5 times greater spatial resolution than 3D-SIM for typical biological samples, making it a great choice for obtaining high structural detail.

The relative thinness of LSECs (150–300 nm) make them ideal candidates for TIRF/HILO (highly inclined and laminated optical sheet) imaging techniques that are typically used in SMLM. This resulted in imaging with low background as the sample thickness is within the z-resolution of single emitters.

Super-resolved imaging of LSECs is, however, a challenging task because multiple experimental parameters have to be considered. The complete membrane has to be stained to observe fenestrations because no specific markers for fenestrations are available. Generally speaking, imaging of tiny holes in biological samples ("negative imaging") is much more demanding compared to, e.g. imaging of the fluorescently labeled cytoskeleton ("positive imaging").

Negative staining requires a significantly lower background to visualize dark areas, which are the objects of interest. To avoid nonspecific binding of fluorophores to the coverslip surface, several washing steps using a mild detergent (0.1% Tween 20) are performed during sample preparation, which we found to have no effect on the membrane of fixed cells [15]. Additionally, the surrounding structure must be labeled with fluorophores as densely as possible. According to the Nyquist-Shannon sampling theorem the mean density of the fluorophores has to be twice as high as the desired resolution. This results in an apparent labeling density of 10^4 molecules/μm^2 to obtain a spatial resolution of 20 nm in 2D. For the same resolution in 3D the density increases to 10^6 molecules/μm^3, which corresponds to a fluorophore concentration in the millimolar range.

As mentioned earlier, *d*STORM applies a Gaussian fit function to a spatially separated fluorescence signal. With increasing labeling density, the probability for non-separated signals rises. This makes an accurate fluorophore position retrieval using only one Gaussian function impossible. In order to process data containing fluorescence signal emitted from connected fluorophores, fitting of multiple Gaussian functions can be performed. Although time-consuming, software packages capable of multiple emitter fitting are available [68, 91].

In the end, localization precision is also crucial, especially for a quantitative data analysis, e.g. to determine the diameter of fenestrations in LSECs. Since Poisson statistics limits localization precision, as many photons as possible have to be collected from each single molecule. Post-processing of the data is very effective at increasing the quality of super-resolved images. Taking only localizations with a rather high precision into account, i.e. rejecting localizations containing photons below a certain threshold value, lowers the total number of localizations. This leads to a reconstructed super-resolved image of lower quality, but longer acquisition times resulting in more raw data images to be processed can easily compensate for this.

The challenge lies then in finding a photoswitchable fluorophore that offers dense and evenly distributed plasma membrane staining to best observe the negative contrast. We found that by using an OSS in combination with cysteamine [62], an increased concentration of another variant of the CellMask stain family, CellMask DeepRed (5 µg/ml), can be used for SMLM as shown in Figure 6. An example for the *d*STORM reconstruction of an entire isolated rat LSEC is shown in Figure 6A. In this super-resolved image the characteristic cellular substructures can be clearly identified. The cell contains a large number of sieve plates with diameters of up to several microns. Each sieve plate contains tens of well-defined fenestrations in the plasma membrane with a mean diameter of about 120 nm (Figure 6B). The wide-field fluorescence image, on the other hand, is almost featureless with dark regions embedded in brighter surroundings adumbrating the location of sieve plates. Only by verification with the complementary *d*STORM image can these regions be identified as sieve plates.

Since *d*STORM can, in principle, achieve a localization precision of less than 20 nm, it enables observations of smaller structures than 3D-SIM which is limited to 100 nm. Fenestration diameters below 50 nm can thus still be observed. The quantitative analysis of the pore diameters of SIM and *d*STORM measurements lead to similar results (129 ± 33 nm for 3D-SIM and 120 ± 38 nm for *d*STORM) [15], with *d*STORM exhibiting a more "hexagonal" inner structure of the pores, which appear rounded in 3D-SIM.

These results demonstrate that SMLM is able to replace the more elaborate and expensive procedures required to view fenestrations by SEM (Figure 2). *d*STORM can now be performed even on standard fluorescence microscopes with super-resolution capabilities at very low cost [92]. Alternatively, SR-SIM also offers the possibility to analyze multiple structures simultaneously at high speed using different stains with high chemical specificity. This makes the analysis of LSECs and their nanosized substructures accessible to a much larger range of biomedical research laboratories around the world.

4.2.1 Correlative 3D-SIM and *d*STORM imaging

The higher spatial resolution of *d*STORM is bought by extensive image acquisition times, because it requires the collection of 10,000–50,000 frames compared to just 15 frames per z-slice (3D-SIM). Mönkemöller et al. [89] recently showed the advantage of combining two complementary super-resolution techniques if the targets of interest, such as the cellular fenestrations of LSECs in the study, are only visible at resolutions well below

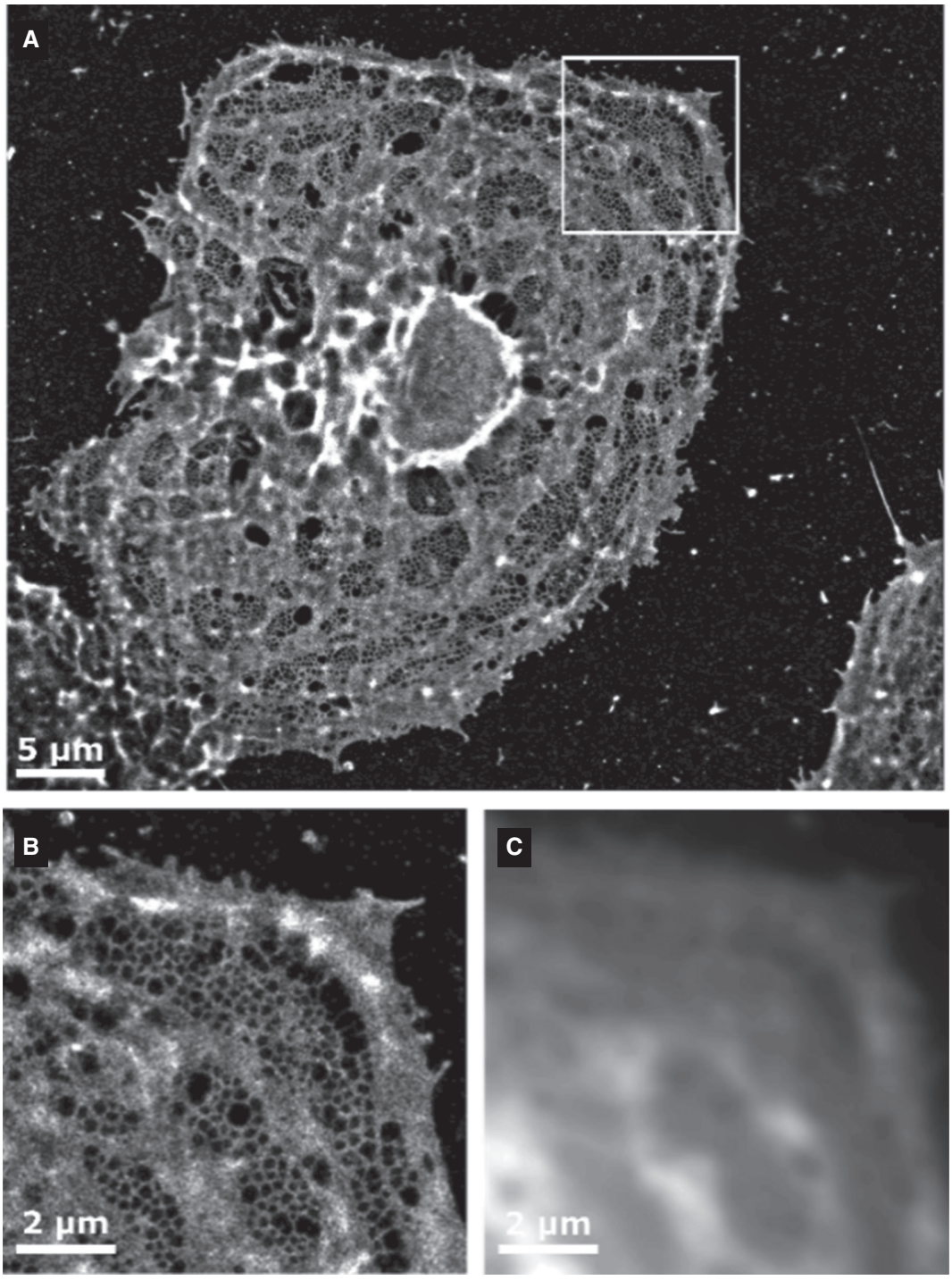

Figure 6: Single molecule localization microscopy reveals nanopores in the cellular plasma membrane.
(A) *d*STORM image of a LSEC plated on a fibronectin-coated glass coverslip, stained with 5 µg/ml CellMask Deep Red, and post-fixed with 3.7% paraformaldehyde. The single frame exposure time was 29.55 ms, and a total of 13,483 frames were used in this reconstruction, resulting in a total acquisition time of about 7 min. The region highlighted in (A) is shown magnified in (B) and compared to the conventional wide-field microscopy image (C). Sieve plates and individual fenestrations can be seen as dark spots against the bright background from the plasma membrane. Taken from [15].

the optical diffraction limit. In this study a multi-modal approach for imaging LSECs combines the rapid search mode over large areas (up to hundreds of microns) by 3D-SIM that enables the identification of relevant features, e.g. fenestrations, followed by the more time consuming and higher resolving *d*STORM imaging of regions

of interest on a single imaging platform. Other groups combined SIM and SMLM [93–95]. However, such a combination of 3D-SIM and *d*STORM, to take advantage of the specific strengths of each technique (rapid, multi-color 3D-SIM search and stitch mode to survey large samples), had not been utilized.

A correlative analysis of 3D-SIM and *d*STORM requires a switching buffer system that is suitable for both super-resolution methods. The chemical environment is crucial to facilitate successful *d*STORM reconstructions, and most measurements are therefore conducted using OSS buffers. In contrast, 3D-SIM imaging requires mounting media with well-adjusted index of refraction that enables aberration-reduced imaging of cells, e.g. *Vectashield*. Olivier et al. [96] recently characterized Vectashield as an excellent switching buffer for certain dyes such as Alexa Fluor 647. Shim et al. [97] describe DiI and DiD as plasma membrane stains with excellent photoswitching behavior under standard buffer conditions, while Mönkemöller et al. [89] showed the ability of using DiD in Vectashield for *d*STORM imaging of negative structures (Figure 7C). In contrast to the plasma membrane stain CellMask (Figure 6), DiD has higher specificity for cell membranes and shows extremely low background.

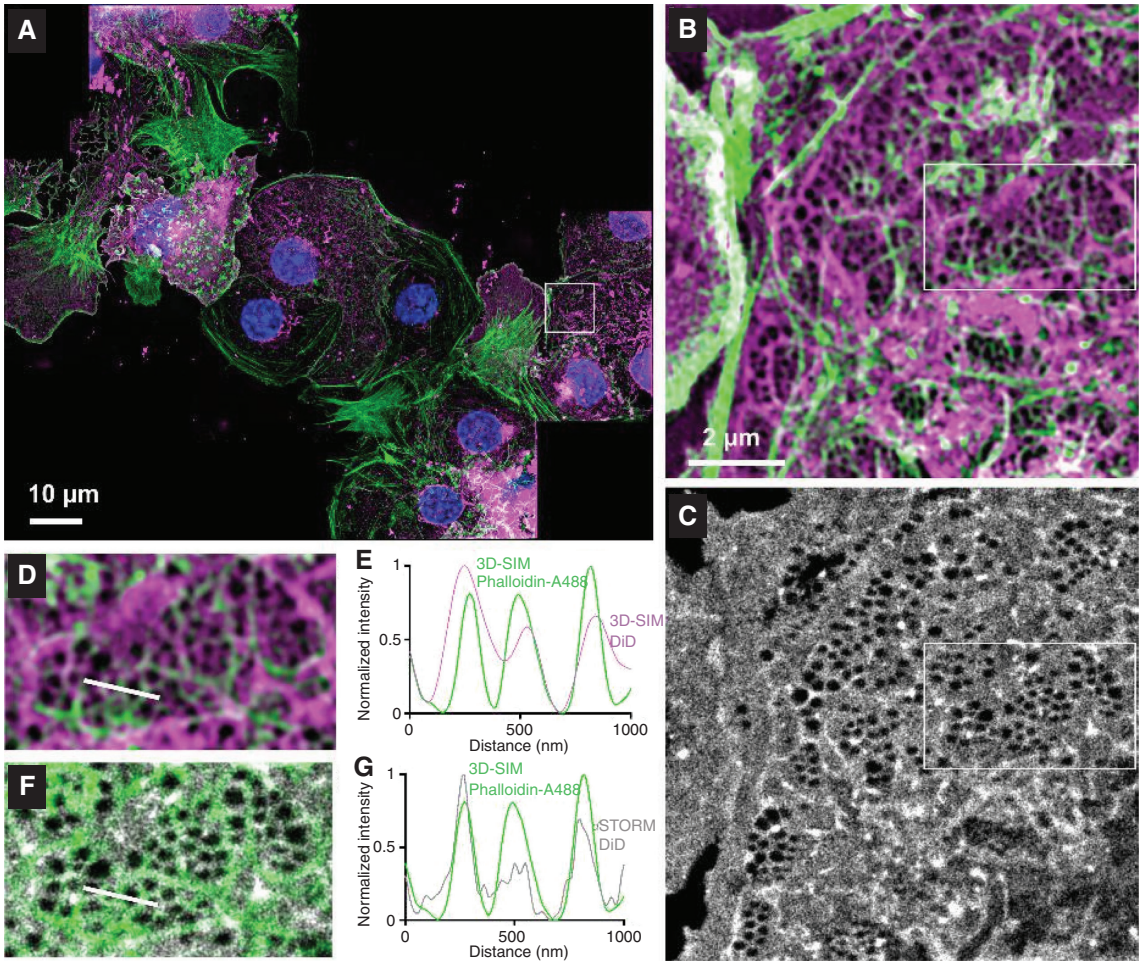

Figure 7: Comparison of cellular features imaged by different super-resolution microscopy modalities.
(A) Nine multi-color maximum intensity z-projection 3D-SIM images of fixed rat LSECs were stitched together to produce this overview image. The cells were stained for nuclei (DAPI, blue), actin (Phalloidin-AF488, green) and membrane (DiD, magenta). (B) Enlarged 3D-SIM view of the ROI shown in (A) highlighting how fenestrations are surrounded by actin fibers. (C) Is the corresponding *d*STORM image of the DiD membrane channel. (D) Is an enlarged view of the ROI shown in (B). (E) Plot of the line section shown in (D) comparing the actin (green) and membrane (magenta) channels of the 3D-SIM image. (F) Overlay of the actin channel from 3D-SIM (D) shown in green and the membrane channel of *d*STORM (C, outlined box) shown in gray. (G) Plot of the line section shown in (F) comparing the 3D-SIM actin (green) and *d*STORM membrane (gray) channels. (G) The actin line (green) shows the same trend as the membrane *d*STORM line (gray), which suggests that actin filaments support fenestrations. Taken from [89].

This multimodal imaging is shown in Figure 7 on fixed, freshly isolated rat LSECs, which are stained for nuclei (blue, DAPI), actin (green, Phalloidin-AF488), and membranes (magenta, DiD) to analyze the connection between the plasma membrane of the fenestrations and the actin cytoskeleton. 3D-SIM imaging offered the fast survey over a large area as shown in Figure 7A. A comparison of the 3D-SIM and *d*STORM images of a region of interest (ROI) is depicted in Figure 7B and C. The cross-modality correlation of a sieve plate imaged by both super-resolution optical methods enables one to directly compare the association between the LSEC cytoskeleton and the plasma membrane (Figure 7F). The actin cytoskeleton colocalizes well with the membrane stain obtained by *d*STORM (Figures 7G and 7F), while the 3D-SIM membrane signal lacks the resolution to truly make this conclusion (Figure 7D and E).

In conclusion, 3D-SIM and *d*STORM have advantages that can significantly improve studies of subcellular ultrastructures of LSECs and other biological systems [98] by combining both techniques to reduce their respective disadvantages.

4.2.2 Correlative chip-based optical nanoscopy with *d*STORM

A novel (and potentially game-changing) illumination method has recently been used for *d*STORM. Diekmann et al. [99] used photonic chips as substrates for *d*STORM imaging of LSECs. To avoid out-of-focus light, in conventional *d*STORM a high NA high magnification TIRF objective lens is used to generate an evanescent field for exciting fluorescent molecules. The same TIRF objective lens is used to excite and to the collect the fluorescence signal from the sample. Therefore, in conventional *d*STORM the f-o-v is limited (typically $50 \times 50\ \mu m^2$) due to the high magnification of the TIRF objective lens. Diekmann et al. [99], however, instead used a waveguide chip to hold and to illuminate the sample to obtain super-resolution images (Figure 8A). The light was coupled into an optical waveguide and was guided to the imaging area by total internal reflection [100]. The evanescent field present on top of the waveguide surface illuminated the sample, and the fluorescence signals from the sample were imaged using an ordinary objective lens (Figure 8B and C). High intensity

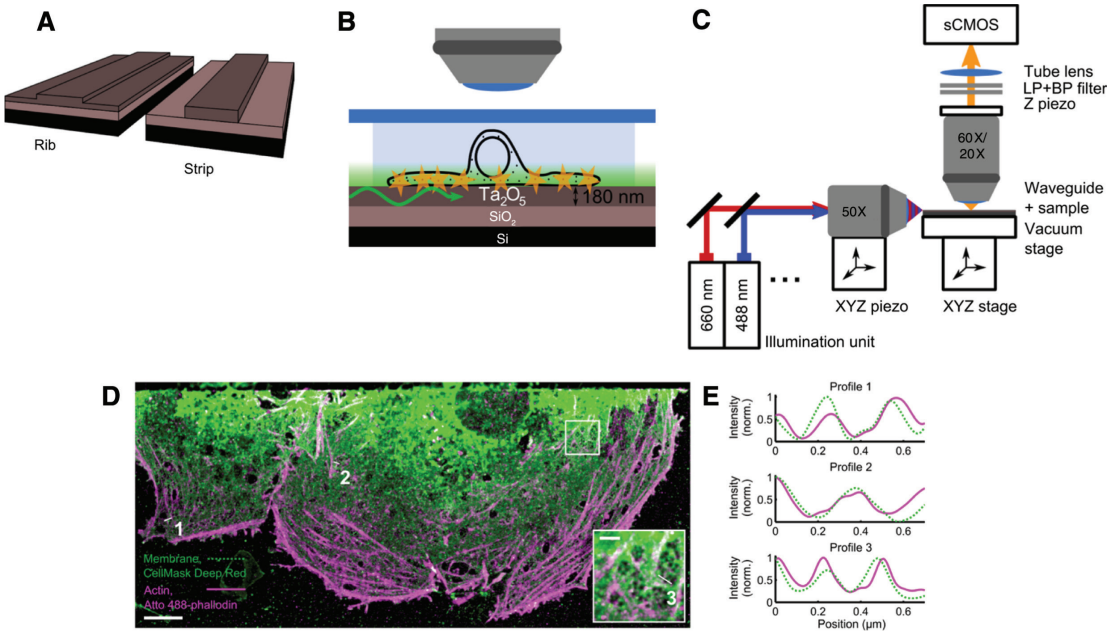

Figure 8: Chip-based nanoscopy.
(A) Schematic diagram of optical waveguide made of either rib or strip geometry. (B) The evanescent field generated on top of tantalum pentoxide (Ta_2O_5) is used to excite the sample. (C) The setup consists of an upright microscope for fluorescence detection and an illumination unit to provide coupling to the input facet of the waveguides. The illumination and collection light path is thus decoupled in chip-based nanoscopy techniques. (D) and (E) Dual color chip-based *d*STORM reveals the interplay between actin (magenta) and the plasma membrane (green) in LSECs. (D) Groups of fenestrations form sieve plate superstructures that are surrounded by actin bundles. The inset shows that actin is present between neighboring fenestrations where it colocalizes with the plasma membrane (scale bar, 5 μm and the scale bar on inset, 1 μm), (E) The line profiles taken at different positions in the liver cell as shown in (E) reveal diameters of approximately 200 nm. Figures taken from [99] and used with permission.

(0.5–10 KW/cm^2) in the evanescent field above the waveguide is desirable to induce blinking of single molecules and is a prerequisite for SMLM. This was achieved by using high-refractive index contrast waveguide material (such as tantalum pentoxide, Ta_2O_5) and by fabricating a thin waveguide geometry (100–200 nm). Different waveguide geometries (rib and strip, Figure 8A and B) were used for chip-based optical nanoscopy. LSECs were directly grown on top of waveguides and similar to how the samples are prepared on top of glass coverslips. The fenestrations in LSECs were imaged with a water immersion 1.2 N.A. 60X objective lens (Figure 8D and E) using an upright optical microscope setup. The optical resolution of 50 nm was reported using chip-based *d*STORM setup. Multi-color chip-based *d*STORM imaging was performed on LSECs to image the interaction between the actin network and fenestrations (Figure 8D and E). It was thus further confirmed that actin filaments colocalize with the membrane supporting both individual fenestrations and sieve plates.

Chip-based optical nanoscopy decouples the illumination and the collection light paths such that the generation of the evanescent field is independent of the collection objective lens (see Figure 8C). This enables the acquisition of super-resolved LSEC images over an extraordinarily large f-o-v using a lower magnification objective lens. Using an optical waveguide of 0.5 mm width and an objective lens of 20X 0.45 N.A, an f-o-v of 0.5×0.5 mm was imaged with an optical resolution of 140 nm. The use of waveguide illumination has the potential to revolutionize nanoscopy in that waveguide slides/chambers can be used to retrofit standard diffraction limited microscopes, turning them into nanoscopes for a fraction of the cost of commercial nanoscopy systems. And, although coupling lasers to waveguides is not (yet) a trivial exercise, they still represent a significant reduction in complexity compared to the bulky optomechanics of nanoscopes available on the market today.

5 Optical nanoscopy and liver sections

The need of having to isolate LSECs and plate them on glass substrates comes with the typical disadvantages of cell culture model systems. The vastly different isolation protocols leading to the separation of LSECs from the liver can also carry uncertainties in the state and nature of the isolated cells [101, 102]. Studying LSECs, and other liver cells, in their more biologically relevant *in vivo* tissue environment will thus always be necessary to confirm the relevance of *in vitro* cell culture findings. Optical nanoscopy might also prove to be a useful diagnostic tool for mitochondrial hepatopathies, such as those in Alpers disease and non-alcoholic liver disease or caused by certain drugs and toxins, metal overload, and alcoholic liver injury [103]. Optical nanoscopy would provide sufficient spatial resolution to determine changes in mitochondrial morphology, such as mitochondrial hyperplasia/megamitochondria, that currently require EM methods to be visualized.

TEM and SEM are two extremely powerful (non-optical) super-resolution methods that have revealed much of the liver's ultrastructure (down to 1–2 nm resolution), including fenestrations on LSECs [14]. And TEM on 70 nm thick patient biopsies is required for diagnosis of numerous diseases of the nervous system, muscles, airways, and kidney because of the 1–2 nm resolution needed. However, EM methods require expensive equipment and specialist staff; they are costly and time consuming to the point where sample preparation and analysis can take up to a week. Much of this can also be said of current optical nanoscopy technologies, although Pullman et al. [104] have used 1–2 h on SIM to perform analysis on human kidney sections that would otherwise take 1–2 days with TEM imaging. Given that the price of optical nanoscopes is decreasing rapidly, and that "home-built" *d*STORM setups are accessible for a tenth of the cost of commercial systems, we anticipate that *d*STORM technology will lend itself to the research and clinical study of liver tissue sections and the fenestrations within. However, to the best of our knowledge, there are no studies yet performed where liver sections have been successfully examined with super-resolution optical methods in a clinical or research setting.

There are, nevertheless, numerous studies using nanoscopy methods (SIM, STORM, and STED) to analyze tissue sections from kidney [104–108], brain/spinal cord [108–113], acute brain slices [114–116], cardiac muscle [108, 117–120], and rectal cancer tissue [121], to name a few. A variety of methods for tissue preparation and fixation were used in these studies, and these can readily be applied to fixed and possibly living liver tissue. In addition, Willig et al. [122] performed STED microscopy on living mouse brain, and adapting this methodology could be an exciting method to study the liver *in vivo*. Using optical nanoscopy to image tissues is, however, challenging due to scattering, aberrations, and absorption that occurs in extended tissue and thus requires specific methodologies to cope with these issues. These can be broadly grouped under two categories, (1) *single photon optical nanoscopy* for imaging thin tissue samples and (2) *multi-photon optical nanoscopy* for imaging thick tissues samples. For thin biopsy sections (typically ≤4 μm thick), many of the existing optical nanoscopy techniques can be applied with static correction methods, such

as collar correction of the objective lens. More complex aberration correction strategies, such as adaptive optics, are required for imaging deeper into tissues. When scattering is significant, two-photon methods can be coupled with optical nanoscopy. The various optical super-resolution methods are outlined below.

5.1 One-photon excitation nanoscopy on thin tissue sections

5.1.1 *d*STORM

*d*STORM (and its equivalent photoactivated localization microscopy: PALM) have been used by Christian Soeller and colleagues to visualize calcium release channels (ryanodine receptors) in 5–10 μm thick cryosections of rat and human cardiac muscle down to 30 nm resolution, i.e. the size of a single receptor [117–119]. A TIRF objective was used in these studies to avoid autofluorescence (AF) from regions outside the focal plane. Specht et al. [110] used *d*STORM/PALM to visualize gephyrin scaffolds in inhibitory synapses in formaldehyde fixed rat spinal cord 0.5–1 μm sections and attained localization precision greater than 15 nm. Similar resolution was achieved by Dani et al. [109] in their study of brain synapses in snap-frozen and formaldehyde fixed 10 μm sections of mouse brain tissue. Yu et al. [107] and Suleiman et al. [105] combined STORM with EM to study kidney podocyte effacement and kidney glomerular basement membrane structure in formaldehyde fixed/frozen sections of 8 μm and 200 nm thickness, respectively, and attained resolutions >30 nm. Given the utility of STORM in such a variety of tissues, this method should lend itself to the successful study of frozen liver sections from 200 nm to 10 μm in thickness.

5.1.2 SIM

Best et al. [123] and Rossberger et al. [93] showed that SIM can be useful for formaldehyde fixed paraffin embedded biopsies with strong AF. Significant resolution enhancement was obtained using SIM on 4 μm thick human eye tissues prepared in paraffin. Another distinct advantage of applying SIM to AF tissue samples was the reduction of the out-of-focus light due to optical section capabilities for the SIM technique. Pullman et al. [104] used SR-SIM as a novel approach to study 5 μm thick frozen normal and nephrotic kidney sections stained with anti-podocin. This method provided sufficient resolution to visualize enlarged podocyte foot processes, as well as the complete loss of these (a.k.a. effacement), seen in nephritis. TEM is the usual diagnostic method to determine nephritic disease in kidney sections. However, the SR-SIM protocol took 1–2 h as opposed to TEM, which takes 1–2 days and requires trained specialists. So, although (in its linear form) SR-SIM resolution is limited to >100 nm, its relative ease of use and compatibility with the majority of fluorophores can make it a very useful tool in the clinical and research setting for the study of liver. Non-linear implementations of SR-SIM, which achieve even greater resolution [82], may further improve its utility in this context. The need for the formation of interference patterns with high contrast in tissue is, however, difficult to achieve in tissue sections thicker than 4 μm.

5.1.3 STED

STED microscopy has been widely applied for imaging brain tissues, including imaging filamentous actin in cortical dendrites of a living mouse [122], and tau filaments 20 μm inside thin cortical gray matter (50 μm formalin fixed brain sections) have been imaged with a resolution of 77 nm using STED by applying static collar correction from the objective lens [113]. Multi-color STED microscopy, achieving 40 nm lateral resolution, has also been applied on 4 μm rat brain tissue sections [112]. And perhaps of greatest interest in the clinical setting is the use of STED to examine paraffin embedded human rectal tissue from biopsies taken 1, 11, and 17 years previously and stored at room temperature during this time [121]. In this study, sub-mitochondrial protein (TOM20, Mic60, aconitase, and cyclophilin D) distribution in mitochondria was investigated, and a resolution of ≈40 nm was typically attained from 2 μm thick sections.

For thicker tissue samples where the scattering and aberrations are predominant, adaptive optics can be applied to correct for more complex aberrations. Adaptive optics has been applied together with 3D-STED microscopy to image 100 nm beads layered under 14–25 μm zebrafish retina sections [124]. Using these methods, the authors managed to resolve the beads down to 140 nm.

5.2 Optical nanoscopy on thick tissues/tissue sections

5.2.1 Two-photon excitation optical nanoscopy

Two-photon excitation of fluorescence as a diffraction limited microscopy technique has been routinely used

for the last two decades for imaging tissue samples. After the invention of optical nanoscopy, researchers have integrated two-photon techniques with optical nanoscopy for imaging highly scattering samples such as tissue samples.

5.2.2 Two-photon STED

STED microscopy was first merged with two-photon excitation to study cultured PtK2 cells [125], and later it was shown that this combination can provide super-resolution imaging up to 100 μm deep inside acute brain slices of 300–350 μm with resolutions between 60 and 100 nm, depending on the depth [114–116]. This method could be promising for the study of liver needle punch biopsies, either fixed or kept alive in media.

5.2.3 Two-photon iSIM

By marrying two-photon excitation with instant iSIM or photon reassignment (a method that improves the spatial resolution of confocal microscopes, when multichannel detectors, such as cameras, are used), Winter et al. [126] reported imaging tissues and organs up to 100 μm deep inside zebrafish embryos to obtain optical resolutions of 140 nm (lateral) and 450 nm (axial). Ingaramo et al. [127] used two-photon multi-focal iSIM to image bile canaliculi in mouse liver tissues. However, as liver tissue is nearly opaque and highly scattering, super-resolution imaging of liver tissue is very challenging. Even two-photon based SIM could not obtain images beyond 25 μm deep inside the liver, and these were not of super-resolution quality.

5.2.4 Optical clearing

Another promising route for applying optical nanoscopy deep inside thick tissue sections is by taking advantage of optical clearing techniques. Optically cleared tissue samples considerably reduce the scattering points and aberration issues. Unnersjö-Jess used optical clearing combined with STED to super resolve podocyte foot processes in 0.8–1.5 mm thick kidney slices. Ke et al. [128] used STED, SIM, and PALM/STORM microscopy on optically cleared brain tissues to obtain high-resolution imaging with an unprecedented optical resolution of up to 50 nm, up to 120 μm deep inside optically cleared brain tissues. Optical clearing could be useful for the study of the liver, assuming that membranes remain intact.

6 Future perspectives

Mainstream laboratories have so far been slow to adopt the above methods, which require significant investments in hardware and training. Currently, the majority of nanoscopes are located within physics/optics laboratories, with most bio-laboratories preferring confocal modalities. That said, the cost of ownership of optical nanoscopes is rapidly decreasing, and home-built *d*STORM systems can now be built at a 10th of the cost of commercial systems. We thus expect that within the next 10 years all commercially available optical microscopes will have some super-resolution capability. Each nanoscopy modality discussed in this review (SIM, *d*STORM, and STED) each have their respective advantages and disadvantages, and there is no “one size fits all” approach. In addition, current nanoscopes are not (yet) suitable for unassisted use at core facilities, which is a significant barrier to their widespread adoption in the life sciences and the clinic. However, with continued development, nanoscopes will become the user-friendly machines that core facility managers can leave in the hands of unassisted users and of standard use in hospital settings.

7 Conclusions

Current optical nanoscopes are able to resolve biological structures, stained with multiple reagents and flurophores, down to 20 nm. This offers several important benefits for their application to fenestrated endothelial cells over the traditional use of EM, such as reduced sample processing time, reduced cost of sample preparation and imaging, and the ability to image wet samples rather than samples in vacuum, which in turn reduces potential preparation and imaging artifacts. Furthermore, fluorescent nanoscopy permits imaging in multiple color channels, and as the greatest benefit, it currently provides the greatest potential for live cell imaging. We are already able to use *d*STORM and SR-SIM nanoscopes to visualize fenestrations in fixed (*d*STORM and SR-SIM) and living (SR-SIM, publication in preparation) LSECs, which was previously only achievable with EM or AFM on fixed cells and liver sections. A natural extension will be to test STED on cultured LSECs and to test all three modalities on liver sections, acute liver slices, and even intact livers, both fixed and *in vivo*. EM, with its superior resolution, will continue to play a vital role in the study of liver cell fenestrations, but nanoscopy will expand our options and enable us to study fixed (but wet) and living LSEC, in multiple contexts.

Acknowledgments: For work at the Arctic University of Norway, University of Tromsø was supported by the Tromsø Research Foundation (supported by Trond Mohn) and a grant from the Department of Medical Biology (UiT) to PM. This work was supported by the European Research Council (grant no. 336716 to BSA), the Research Council of Norway (grant no. 244764/F11 to BSA), and the German Academic Exchange Service (grant no. 57160327 to MS). TH acknowledges grant no. INST 215/435-1 FUGG from the DFG. This work was supported in parts by the Ministry of Innovation, Science, Research and Technology of the State of North Rhine-Westphalia (MIWFT) as part of the research cooperation "MoRitS – Model- based Realization of intelligent Systems in Nano- and Biotechnologies" (grant no. 321-8.03.04.03-2012/02). This work receives funding from the European Union's Horizon 2020 research and innovation programme under the Marie Sklodowska-Curie grant agreement no. 766181, project "DeLIVER".

Abbreviations

AFM	Atomic force microscopy
AF	Autofluorescence
*d*STORM	*Direct* stochastic optical reconstruction microscopy
EM	Electron microscopy
fPALM	Fluorescence photoactivation localization microscopy
FWHM	Full width at half maximum
HILO	Highly inclined and laminated optical sheet
LSECs	Liver sinusoidal endothelial cells
LSM	Laser scanning microscopy
NA	Numerical aperture
NL-SIM	Non-linear structured illumination microscopy
OTF	Optical transfer function
PA-GFP	Photoactivable green fluorescent protein
PALM	Photoactivated localization microscopy
PSF	Point spread function
ROI	Region of interest
SERS	Surface-enhanced Raman scattering
SIM	Structured illumination microscopy
STED	Stimulated emission depletion
TEM	Transmission electron microscopy
SEM	Scanning electron microscopy
SMLM	Single molecule localization microscopy
SR-SIM	Super-resolution structured illumination microscopy
TIRF	Total internal reflection fluorescence

References

[1] Sorensen KK, Simon-Santamaria J, McCuskey RS, Smedsrod B. Liver sinusoidal endothelial cells. Compr Physiol 2015;5: 1751–74.

[2] Blumgart LH. Surgery of the liver, biliary tract, and pancreas. 3rd ed. Philadelphia, Saunders Elsevier, 2007, 3–30.

[3] Baynes JW, Dominiczak MH. Medical biochemistry. 2nd ed. Philadelphia, Elsevier Mosby, 2005, xii, 693.

[4] Kmiec Z. Cooperation of liver cells in health and disease. Adv Anat Embryol Cell Biol 2001;161:1–151.

[5] Marieb EN, Hoehn KN. Human Anatomy & Physiology. 9th ed, Pearson Education, Inc. United States of America, 2013.

[6] MacPhee PJ, Schmidt EE, Groom AC. Intermittence of blood flow in liver sinusoids, studied by high-resolution in vivo microscopy. Am J Physiol 1995;269:G692–8.

[7] Wisse E, De Zanger RB, Jacobs R, McCuskey RS. Scanning electron microscope observations on the structure of portal veins, sinusoids and central veins in rat liver. Scan Electron Microsc 1983;(Pt 3):1441–52.

[8] Sorensen KK, McCourt P, Berg T, et al. The scavenger endothelial cell: a new player in homeostasis and immunity. Am J Physiol Regul Integr Comp Physiol 2012;303:R1217–30.

[9] Wisse E, De Zanger RB, Charels K, Van Der Smissen P, McCuskey RS. The liver sieve: considerations concerning the structure and function of endothelial fenestrae, the sinusoidal wall and the space of Disse. Hepatology 1985;5:683–92.

[10] Wake K. Perisinusoidal stellate cells (fat-storing cells, interstitial cells, lipocytes), their related structure in and around the liver sinusoids, and vitamin A-storing cells in extrahepatic organs. Int Rev Cytol 1980;66:303–53.

[11] Wake K, Decker K, Kirn A, et al. Cell biology and kinetics of Kupffer cells in the liver. Int Rev Cytol 1989;118:173–229.

[12] McLean AJ, Cogger VC, Chong GC, et al. Age-related pseudocapillarization of the human liver. J Pathol 2003;200:112–7.

[13] Braet F, Wisse E. Structural and functional aspects of liver sinusoidal endothelial cell fenestrae: a review. Comp Hepatol 2002;1:1.

[14] Wisse E. An electron microscopic study of the fenestrated endothelial lining of rat liver sinusoids. J Ultrastruct Res 1970;31:125–50.

[15] Mönkemöller V, Schuttpelz M, McCourt P, Sorensen K, Smedsrod B, Huser T. Imaging fenestrations in liver sinusoidal endothelial cells by optical localization microscopy. Phys Chem Chem Phys 2014;16:12576–81.

[16] Braet F, Riches J, Geerts W, Jahn KA, Wisse E, Frederik P. Three-dimensional organization of fenestrae labyrinths in liver sinusoidal endothelial cells. Liver Int 2009;29:603–13.

[17] Braet F, Wisse E, Bomans P, et al. Contribution of high-resolution correlative imaging techniques in the study of the liver sieve in three-dimensions. Microsc Res Tech 2007;70: 230–42.

[18] DeLeve LD. Liver sinusoidal endothelial cells in hepatic fibrosis. Hepatology 2015;61:1740–6.

[19] Farrell GC, Teoh NC, McCuskey RS. Hepatic microcirculation in fatty liver disease. Anat Rec (Hoboken) 2008;291:684–92.

[20] Fraser R, Cogger VC, Dobbs B, et al. The liver sieve and atherosclerosis. Pathology 2012;44:181–6.

[21] Mori T, Okanoue T, Sawa Y, Hori N, Ohta M, Kagawa K. Defenestration of the sinusoidal endothelial-cell in a rat model of cirrhosis. Hepatology 1993;17:891–7.

[22] Warren A, Bertolino P, Benseler V, Fraser R, McCaughan GW, Le Couteur DG. Marked changes of the hepatic sinusoid in a transgenic mouse model of acute immune-mediated hepatitis. J Hepatol 2007;46:239–46.

[23] Steffan AM, Pereira CA, Bingen A, et al. Mouse hepatitis-virus type-3 infection provokes a decrease in the number of sinusoidal endothelial-cell fenestrae both in-vivo and in-vitro. Hepatology 1995;22:395–401.
[24] Dobbs BR, Rogers GWT, Xing HY, Fraser R. Endotoxin-induced defenestration of the hepatic sinusoidal endothelium – a factor in the pathogenesis of cirrhosis. Liver 1994;14:230–3.
[25] Le Couteur DG, Cogger VC, Markus AMA, et al. Pseudocapillarization and associated energy limitation in the aged rat liver. Hepatology 2001;33:537–43.
[26] Mohamad M, Mitchell SJ, Wu LE, et al. Ultrastructure of the liver microcirculation influences hepatic and systemic insulin activity and provides a mechanism for age-related insulin resistance. Aging Cell 2016;15:706–15.
[27] Le Couteur DG, Fraser R, Cogger VC, McLean AJ. Hepatic pseudocapillarisation and atherosclerosis in ageing. Lancet 2002;359:1612–5.
[28] Cogger VC, Svistounov D, Warren A, et al. Liver aging and pseudocapillarization in a Werner syndrome mouse model. J Gerontol A Biol Sci Med Sci 2014;69:1076–86.
[29] Cogger VC, Warren A, Fraser R, Ngu M, McLean AJ, Le Couteur DG. Hepatic sinusoidal pseudocapillarization with aging in the non-human primate. Exp Gerontol 2003;38:1101–7.
[30] Hilmer SN, Cogger VC, Fraser R, McLean AJ, Sullivan D, Le Couteur DG. Age-related changes in the hepatic sinusoidal endothelium impede lipoprotein transfer in the rat. Hepatology 2005;42:1349–54.
[31] Warren A, Bertolino P, Cogger VC, McLean AJ, Fraser R, Le Couteur DG. Hepatic pseudocapillarization in aged mice. Exp Gerontol 2005;40:807–12.
[32] O'Reilly JN, Cogger VC, Le Couteur DG. Old age is associated with ultrastructural changes in isolated rat liver sinusoidal endothelial cells. J Electron Microsc (Tokyo) 2010;59:65–9.
[33] Le Couteur DG, Warren A, Cogger VC, et al. Old age and the hepatic sinusoid. Anat Rec 2008;291:672–83.
[34] Warren A, Cogger VC, Fraser R, Deleve LD, McCuskey RS, Le Couteur DG. The effects of old age on hepatic stellate cells. Curr Gerontol Geriatr Res 2011;2011:439835.
[35] Crang RFE, Klomparens KL. Artifacts in biological electron microscopy. Science 1988;242:309.
[36] Bouwens L, Wisse E. Proliferation, kinetics, and fate of monocytes in rat liver during a zymosan-induced inflammation. J Leukoc Biol 1985;37:531–43.
[37] Parot P, Dufrene YF, Hinterdorfer P, et al. Past, present and future of atomic force microscopy in life sciences and medicine. J Mol Recognit 2007;20:418–31.
[38] Braet F, DeZanger R, Kammer S, Wisse E. Noncontact versus contact imaging: an atomic force microscopic study on hepatic endothelial cells in vitro. Int J Imag Syst Tech 1997;8:162–7.
[39] Braet F, Wisse E. AFM imaging of fenestrated liver sinusoidal endothelial cells. Micron 2012;43:1252–8.
[40] Zapotoczny B, Owczarczyk K, Szafranska K, Kus E, Chlopicki S, Szymonski M. Morphology and force probing of primary murine liver sinusoidal endothelial cells. J Mol Recognit 2017;30:e2610.
[41] Hell SW, Wichmann J. Breaking the diffraction resolution limit by stimulated-emission – stimulated-emission-depletion fluorescence microscopy. Opt Lett 1994;19:780–2.
[42] Hell SW. Toward fluorescence nanoscopy. Nat Biotechnol 2003;21:1347–55.
[43] Betzig E, Patterson GH, Sougrat R, et al. Imaging intracellular fluorescent proteins at nanometer resolution. Science 2006;313:1642–5.
[44] Bates M, Huang B, Zhuang XW. Super-resolution microscopy by nanoscale localization of photo-switchable fluorescent probes. Curr Opin Chem Biol 2008;12:505–14.
[45] Gustafsson MG. Surpassing the lateral resolution limit by a factor of two using structured illumination microscopy. J Microsc 2000;198:82–7.
[46] Abbe E. Beiträge zur Theorie des Mikroskops und der mikroskopischen Wahrnehmung. Archiv für mikroskopische Anatomie 1873;9:413–8.
[47] Pawley JB. Handbook of biological confocal microscopy. 3rd ed. New York, NY, Springer, 2006, xxviii, 985.
[48] Abrahamsson S, Ball G, Wicker K, Heintzmann R, Schermelleh L. Structured illumination microscopy. In: Diaspro A, van Zandvoort MAMJ, eds. Super-Resolution Imaging in Biomedicine, Boca Raton, FL, USA, CRC Press, 2016, 137–47.
[49] Heintzmann R, Cremer CG. Laterally modulated excitation microscopy: improvement of resolution by using a diffraction grating. BiOS Europe'98. 1999. SPIE Proceedings, Volume 3568, p. 185–196.
[50] Gustafsson MG, Shao L, Carlton PM, et al. Three-dimensional resolution doubling in wide-field fluorescence microscopy by structured illumination. Biophys J 2008;94:4957–70.
[51] Mönkemöller V. Optical super-resolution microscopy of the structure and dynamics of cellular nanopores [PhD thesis]: Bielefeld University, 2016.
[52] Muller M, Monkemoller V, Hennig S, Hubner W, Huser T. Open-source image reconstruction of super-resolution structured illumination microscopy data in ImageJ. Nat Commun 2016;7:10980.
[53] Ball G, Demmerle J, Kaufmann R, Davis I, Dobbie IM, Schermelleh L. SIMcheck: a toolbox for successful super-resolution structured illumination microscopy. Sci Rep 2015;5:15915.
[54] Hess ST, Girirajan TP, Mason MD. Ultra-high resolution imaging by fluorescence photoactivation localization microscopy. Biophys J 2006;91:4258–72.
[55] Rust MJ, Bates M, Zhuang X. Sub-diffraction-limit imaging by stochastic optical reconstruction microscopy (STORM). Nat Methods 2006;3:793–5.
[56] Betzig E. Proposed method for molecular optical imaging. Opt Lett 1995;20:237–9.
[57] Ando R, Mizuno H, Miyawaki A. Regulated fast nucleocytoplasmic shuttling observed by reversible protein highlighting. Science 2004;306:1370–3.
[58] Bates M, Blosser TR, Zhuang X. Short-range spectroscopic ruler based on a single-molecule optical switch. Phys Rev Lett 2005;94:108101.
[59] Heilemann M, Margeat E, Kasper R, Sauer M, Tinnefeld P. Carbocyanine dyes as efficient reversible single-molecule optical switch. J Am Chem Soc 2005;127:3801–6.
[60] Heilemann M, van de Linde S, Mukherjee A, Sauer M. Super-resolution imaging with small organic fluorophores. Angew Chem Int Ed Engl 2009;48:6903–8.
[61] Heilemann M, van de Linde S, Schuttpelz M, et al. Subdiffraction-resolution fluorescence imaging with conventional fluorescent probes. Angew Chem Int Ed Engl 2008;47:6172–6.
[62] van de Linde S, Loschberger A, Klein T, et al. Direct stochastic optical reconstruction microscopy with standard fluorescent probes. Nat Protoc 2011;6:991–1009.

[63] Rasnik I, McKinney SA, Ha T. Nonblinking and long-lasting single-molecule fluorescence imaging. Nat Methods 2006;3:891–3.
[64] Thompson RE, Larson DR, Webb WW. Precise nanometer localization analysis for individual fluorescent probes. Biophys J 2002;82:2775–83.
[65] Deschout H, Cella Zanacchi F, Mlodzianoski M, et al. Precisely and accurately localizing single emitters in fluorescence microscopy. Nat Methods 2014;11:253–66.
[66] Wolter S, Schuttpelz M, Tscherepanow M, van de Linde S, Heilemann M, Sauer M. Real-time computation of subdiffraction-resolution fluorescence images. J Microsc 2010;237:12–22.
[67] Wolter S, Loschberger A, Holm T, et al. rapidSTORM: accurate, fast open-source software for localization microscopy. Nat Methods 2012;9:1040–1.
[68] Ovesny M, Krizek P, Borkovec J, Svindrych Z, Hagen GM. ThunderSTORM: a comprehensive ImageJ plug-in for PALM and STORM data analysis and super-resolution imaging. Bioinformatics 2014;30:2389–90.
[69] Sage D, Kirshner H, Pengo T, et al. Quantitative evaluation of software packages for single-molecule localization microscopy. Nat Methods 2015;12:717–24.
[70] Huang F, Hartwich TM, Rivera-Molina FE, et al. Video-rate nanoscopy using sCMOS camera-specific single-molecule localization algorithms. Nat Methods 2013;10:653–8.
[71] Brede N, Lakadamyali M. GraspJ: an open source, real-time analysis package for super-resolution imaging. Opt Nanoscopy 2012;1:11–7.
[72] Smith CS, Joseph N, Rieger B, Lidke KA. Fast, single-molecule localization that achieves theoretically minimum uncertainty. Nat Methods 2010;7:373–5.
[73] Kechkar A, Nair D, Heilemann M, Choquet D, Sibarita JB. Real-time analysis and visualization for single-molecule based super-resolution microscopy. PLoS One 2013;8:e62918.
[74] Klar TA, Jakobs S, Dyba M, Egner A, Hell SW. Fluorescence microscopy with diffraction resolution barrier broken by stimulated emission. Proc Natl Acad Sci USA 2000;97:8206–10.
[75] Hell SW. Far-field optical nanoscopy. Science 2007;316:1153–8.
[76] Eggeling C, Ringemann C, Medda R, et al. Direct observation of the nanoscale dynamics of membrane lipids in a living cell. Nature 2009;457:1159–62.
[77] Hofmann M, Eggeling C, Jakobs S, Hell SW. Breaking the diffraction barrier in fluorescence microscopy at low light intensities by using reversibly photoswitchable proteins. Proc Natl Acad Sci USA 2005;102:17565–9.
[78] Heintzmann R, Jovin TM, Cremer C. Saturated patterned excitation microscopy – a concept for optical resolution improvement. J Opt Soc Am A 2002;19:1599–609.
[79] Gustafsson MGL. Nonlinear structured-illumination microscopy: wide-field fluorescence imaging with theoretically unlimited resolution. Proc Natl Acad Sci USA 2005;102:13081–6.
[80] Laissue PP, Alghamdi RA, Tomancak P, Reynaud EG, Shroff H. Assessing phototoxicity in live fluorescence imaging. Nat Methods 2017;14:657–61.
[81] Rego EH, Shao L, Macklin JJ, et al. Nonlinear structured-illumination microscopy with a photoswitchable protein reveals cellular structures at 50-nm resolution. Proc Natl Acad Sci USA 2012;109:E135–43.
[82] Li D, Shao L, Chen BC, et al. Extended-resolution structured illumination imaging of endocytic and cytoskeletal dynamics. Science 2015;349:aab3500 1–10.
[83] Li D, Betzig E. Response to comment on "Extended-resolution structured illumination imaging of endocytic and cytoskeletal dynamics". Science 2016;352:527.
[84] Sahl SJ, Balzarotti F, Keller-Findeisen J, et al. Comment on "Extended-resolution structured illumination imaging of endocytic and cytoskeletal dynamics". Science 2016;352:527.
[85] Chu K, McMillan PJ, Smith ZJ, et al. Image reconstruction for structured-illumination microscopy with low signal level. Opt Express 2014;22:8687–702.
[86] Perez V, Chang BJ, Stelzer EH. Optimal 2D-SIM reconstruction by two filtering steps with Richardson-Lucy deconvolution. Sci Rep 2016;6:37149.
[87] Cogger VC, McNerney GP, Nyunt T, et al. Three-dimensional structured illumination microscopy of liver sinusoidal endothelial cell fenestrations. J Struct Biol 2010;171:382–8.
[88] Hennig S, Monkemoller V, Boger C, Muller M, Huser T. Nanoparticles as nonfluorescent analogues of fluorophores for optical nanoscopy. ACS Nano 2015;9:6196–205.
[89] Mönkemöller V, Oie C, Hubner W, Huser T, McCourt P. Multimodal super-resolution optical microscopy visualizes the close connection between membrane and the cytoskeleton in liver sinusoidal endothelial cell fenestrations. Sci Rep 2015;5:16279.
[90] Svistounov D, Warren A, McNerney GP, et al. The relationship between fenestrations, sieve plates and rafts in liver sinusoidal endothelial cells. PLoS One 2012;7:e46134.
[91] Holden SJ, Uphoff S, Kapanidis AN. DAOSTORM: an algorithm for high- density super-resolution microscopy. Nat Methods 2011;8:279–80.
[92] Holm T, Klein T, Löschberger A, et al. A blueprint for cost-efficient localization microscopy. ChemPhysChem 2014;15:651–4.
[93] Rossberger S, Ach T, Best G, Cremer C, Heintzmann R, Dithmar S. High-resolution imaging of autofluorescent particles within drusen using structured illumination microscopy. Br J Ophthalmol 2013;97:518–23.
[94] Hamel V, Guichard P, Fournier M, et al. Correlative multicolor 3D SIM and STORM microscopy. Biomed Opt Express 2014;5:3326–36.
[95] Matsuda A, Shao L, Boulanger J, et al. Condensed mitotic chromosome structure at nanometer resolution using PALM and EGFP-histones. PLoS One 2010;5:e12768.
[96] Olivier N, Keller D, Rajan VS, Gonczy P, Manley S. Simple buffers for 3D STORM microscopy. Biomed Opt Express 2013;4:885–99.
[97] Shim SH, Xia C, Zhong G, et al. Super-resolution fluorescence imaging of organelles in live cells with photoswitchable membrane probes. Proc Natl Acad Sci USA 2012;109:13978–83.
[98] Schurmann M, Frese N, Beyer A, et al. Helium ion microscopy visualizes lipid nanodomains in mammalian cells. Small 2015;11:5781–9.
[99] Diekmann R, Helle ØI, Øie CI, et al. Chip-based wide field-of-view nanoscopy. Nat Photonics 2017;11:322–8.
[100] Agnarsson B, Ingthorsson S, Gudjonsson T, Leosson K. Evanescent-wave fluorescence microscopy using symmetric planar waveguides. Opt Express 2009;17:5075–82.
[101] Elvevold K, Smedsrod B, Martinez I. The liver sinusoidal endothelial cell: a cell type of controversial and confusing identity. Am J Physiol Gastrointest Liver Physiol 2008;294:G391–400.

[102] Meyer J, Gonelle-Gispert C, Morel P, Buhler L. Methods for isolation and purification of murine liver sinusoidal endothelial cells: a systematic review. PLoS One 2016;11:e0151945.
[103] Treem WR, Sokol RJ. Disorders of the mitochondria. Semin Liver Dis 1998;18:237–53.
[104] Pullman JM, Nylk J, Campbell EC, Gunn-Moore FJ, Prystowsky MB, Dholakia K. Visualization of podocyte substructure with structured illumination microscopy (SIM): a new approach to nephrotic disease. Biomed Opt Express 2016;7:302–11.
[105] Suleiman H, Zhang L, Roth R, et al. Nanoscale protein architecture of the kidney glomerular basement membrane. Elife 2013;2:e01149.
[106] Unnersjö-Jess D, Scott L, Blom H, Brismar H. Super-resolution stimulated emission depletion imaging of slit diaphragm proteins in optically cleared kidney tissue. Kidney Int 2016;89:243–7.
[107] Yu H, Suleiman H, Kim AH, et al. Rac1 activation in podocytes induces rapid foot process effacement and proteinuria. Mol Cell Biol 2013;33:4755–64.
[108] Barna L, Dudok B, Miczan V, Horvath A, Laszlo ZI, Katona I. Correlated confocal and super-resolution imaging by VividSTORM. Nat Protoc 2016;11:163–83.
[109] Dani A, Huang B, Bergan J, Dulac C, Zhuang X. Superresolution imaging of chemical synapses in the brain. Neuron 2010;68:843–56.
[110] Specht CG, Izeddin I, Rodriguez PC, et al. Quantitative nanoscopy of inhibitory synapses: counting gephyrin molecules and receptor binding sites. Neuron 2013;79:308–21.
[111] Dudok B, Barna L, Ledri M, et al. Cell-specific STORM super-resolution imaging reveals nanoscale organization of cannabinoid signaling. Nat Neurosci 2015;18:75–86.
[112] Kempf C, Staudt T, Bingen P, et al. Tissue multicolor STED nanoscopy of presynaptic proteins in the calyx of Held. PLoS One 2013;8:e62893.
[113] Benda A, Aitken H, Davies DS, Whan R, Goldsbury C. STED imaging of tau filaments in Alzheimer's disease cortical grey matter. J Struct Biol 2016;195:345–52.
[114] Bethge P, Chereau R, Avignone E, Marsicano G, Nagerl UV. Two-photon excitation STED microscopy in two colors in acute brain slices. Biophys J 2013;104:778–85.
[115] Ding JB, Takasaki KT, Sabatini BL. Supraresolution imaging in brain slices using stimulated-emission depletion two-photon laser scanning microscopy. Neuron 2009;63:429–37.
[116] Takasaki KT, Ding JB, Sabatini BL. Live-cell superresolution imaging by pulsed STED two-photon excitation microscopy. Biophys J 2013;104:770–7.
[117] Hou Y, Jayasinghe I, Crossman DJ, Baddeley D, Soeller C. Nanoscale analysis of ryanodine receptor clusters in dyadic couplings of rat cardiac myocytes. J Mol Cell Cardiol 2015;80:45–55.
[118] Jayasinghe ID, Munro M, Baddeley D, Launikonis BS, Soeller C. Observation of the molecular organization of calcium release sites in fast- and slow-twitch skeletal muscle with nanoscale imaging. J R Soc Interface 2014;11:pii: 20140570.
[119] Baddeley D, Crossman D, Rossberger S, et al. 4D super-resolution microscopy with conventional fluorophores and single wavelength excitation in optically thick cells and tissues. PLoS One 2011;6:e20645.
[120] Crossman DJ, Ruygrok PN, Hou YF, Soeller C. Next-generation endomyocardial biopsy: the potential of confocal and super-resolution microscopy. Heart Fail Rev 2015;20:203–14.
[121] Ilgen P, Stoldt S, Conradi LC, et al. STED super-resolution microscopy of clinical paraffin-embedded human rectal cancer tissue. PLoS One 2014;9:e101563.
[122] Willig KI, Steffens H, Gregor C, Herholt A, Rossner MJ, Hell SW. Nanoscopy of filamentous actin in cortical dendrites of a living mouse. Biophys J 2014;106:L01–3.
[123] Best G, Amberger R, Baddeley D, et al. Structured illumination microscopy of autofluorescent aggregations in human tissue. Micron 2011;42:330–5.
[124] Gould TJ, Burke D, Bewersdorf J, Booth MJ. Adaptive optics enables 3D STED microscopy in aberrating specimens. Opt Express 2012;20:20998–1009.
[125] Moneron G, Hell SW. Two-photon excitation STED microscopy. Opt Express 2009;17:14567–73.
[126] Winter PW, York AG, Nogare DD, et al. Two-photon instant structured illumination microscopy improves the depth penetration of super-resolution imaging in thick scattering samples. Optica 2014;1:181–91.
[127] Ingaramo M, York AG, Wawrzusin P, et al. Two-photon excitation improves multifocal structured illumination microscopy in thick scattering tissue. Proc Natl Acad Sci USA 2014;111:5254–9.
[128] Ke MT, Nakai Y, Fujimoto S, et al. Super-resolution mapping of neuronal circuitry with an index-optimized clearing agent. Cell Rep 2016;14:2718–32.